SISSA **ISAS**

SCUOLA INTERNAZIONALE SUPERIORE DI STUDI AVANZATI
INTERNATIONAL SCHOOL FOR ADVANCED STUDIES

Variational techniques in the numerical simulation of molecular dynamics trajectories and of wetting on rough surfaces

Thesis submitted for the degree of
"Doctor Philosophiæ"

Supervisor
Prof. Antonio DeSimone

Candidate
Alessandro Turco

October 2008

Il presente lavoro costituisce la tesi presentata da Alessandro Turco, sotto la direzione di ricerca del Prof. Antonio DeSimone, al fine di ottenere l'attestato di ricerca post-universitaria *Doctor Philosophiae in Matematica Applicata* presso la S.I.S.S.A.. Ai sensi dell' art. 18, comma 3, dello Statuto della Sissa pubblicato sulla G.U. no 62 del 15.03.2001, il predetto attestato è equipollente al titolo di *Dottore di Ricerca in Matematica*.

Trieste, Ottobre 2008.

A Elena

Contents

Introduction

This thesis is devoted to the study of two different problems arising from the numerical simulation of physical phenomena. However, the motivation, the method followed and the goals pursued are the same. As I hope to have exhaustively demonstrated in the following pages, my belief is that variational techniques can be the appropriate bridge between theory and experiment, between mathematical modeling and numerical simulation.

Molecular dynamics is a typical field in which all these ingredients are mixed: simulations of atomic and molecular trajectories are performed, through a suitable model of the interatomic forces and following a suitable algorithm, capable to resolve a large number of degrees of freedom. The aim is to obtain results comparable to observations in order to validate the whole strategy and then to use it as a speculative tool.

Wetting phenomena are at a first glance easier, at least because they are closer to our daily experience. Notwithstanding this (or maybe exactly for this reason) many problems remain open and interesting from the research and the industrial point of view.

Dealing with both fields, I worked with the purpose of finding the mathematical answer to the physical problem, through the means of variational techniques that constituted my original background. However, it is necessary to work on both banks in order to build a bridge and therefore my education during the PhD course touched physics, programming, modeling, mathematical and numerical analysis. As a result of this strategy, I cannot say to have explored completely any of these field, but I can surely affirm to have connected the two sides with a solid and useful path. A path that can obviously be further improved, as I will try to explain in the *"perspectives"* sections of this thesis, but it is already considered interesting, as it has been highlighted by the comments received from the reviewers of the submitted papers.

The studies concerning molecular dynamics are the results of a collaboration with Prof. F. Cardin and Dr. D. Passerone started during the preparation of my degree thesis. We focused on the *rare events* problem: we looked for a strategy to simulate the jump of a many-body system between two (local) minima of its potential energy. The difficulties of such a situation are essentially the large number of degrees of freedom and the very long time that an ab-initio simulation would require before describing the jump. Any classical approach, consisting in a smart integration of the equation of motion, fails because of the combination of these two factors and the subsequent lost of accuracy.

An answer to this problem is theoretically known: a variational principle with fixed end points can predict the existence of reactive trajectories. However this kind of solution hides new problems concerning the numerical strategy to make the functional involved stationary, since low order formulations (i.e. not containing second order derivatives, too expensive from the computational point of view) exhibits mechanical solutions almost only as saddle points.

Hence our objective was a variational formulation with an high stability, in order to be able to handle large systems for long times, and a strategy (something more than a simple algorithm) to make possible a numerical treatment of interesting systems.

We did something more. The functional we adapted to the problem is Tonelli functional which moreover allows for a strong conservation of the imposed total energy of the system during the simulations and it divides easily the search for the geometric localization of the path from its time parametrization: only a linear reparametrization will be needed.

The mechanism is very similar to what the most known Maupertuis functional does. The geometric trajectory is found considering a reference time parametrization, say from 0 to 1, and -once obtained it- the real physical timing is derived through a specific relation. But while the reparametrization of Maupertuis functional is nonlinear and it diverges for zero-velocity points, Tonelli formulation is much more stable and simple. The functional reads:

$$\mathcal{T}_h(q(\cdot)) = \int_0^1 K(\dot{q}(\tau))\, d\tau \cdot \int_0^1 (h - V(q(\tau)))\, d\tau \tag{1}$$

and the factor ω for the linear transformation of time is given by:

$$\omega^2 := \frac{\int_0^1 (h - V(q(\tau)))\, d\tau}{\int_0^1 K(\dot{q}(\tau))\, d\tau}. \tag{2}$$

In the above formulas V is the potential energy, the key ingredient coming from the mathematical modeling of the problem, K is the kinetic energy and h is the imposed value for the total energy. The class of admissible trajectories $q(\cdot)$ will be specified in chapter §1 starting from the request of fixed end points belonging to the basins of attraction of the two minima of the potential selected.

The announced strategy for the stationarization of this functional involves another variational technique, an exact finite dimensional reduction, and an algorithm to couple the two tools. The reduction is performed in Fourier coordinates, a non optimal choice on which we are planning part of our future work. The idea is to divide the low frequencies, which will be the unknowns for the saddle point algorithm, from the high ones. These frequencies will be obtained through an iterative contractive map, whose convergence is rigorously proved if the coordinate of the cut in the series satisfies a precise inequality. The result is a consistent decrease of the number of the degrees of freedom for the problem, without loosing accuracy of the description (an error estimate will be proved) but only at the cost of some fixed-point iteration.

Several examples and numerical tests complete the exposition of this work, clarifying once more the details of the whole strategy and of each component. A comparison between Maupertuis and Tonelli functionals is performed on a simple double well potential and on the standard benchmark constituted by Mueller potential. The finite reduction is first applied to an harmonic oscillator in order to explain the meaning of the condition for the cut in the Fourier series. Then the algorithm governing the coupling of the reduction with Tonelli functional is step by step illustrated on a small cluster of 4 atoms. Finally the isomerization of a 38-atom Lennard-Jones is considered and resolved with the proposed strategy showing a first proof of its capabilities. The results just described are contained in paper [A].

I want to remark once more the spirit of this research: finding an answer to a precise question arising in a physical context through a mathematical, variational technique. We reached the goal and at the same time we opened further questions. Our work from now will consists in widening the possibilities of the strategy and in going deeper in the understanding of the problem. The choice of the Fourier representation for example, although necessary for the technique, is far from being numerically convenient with respect to splines or simply cartesian coordinates. Moreover an a priori guess on the existence of reactive trajectories at given energies would be very useful. Finally we are investigating the possibility of widening the system treatable with these techniques or equivalently the possibility to modify the

algorithms.

Chapter §2, §3 and §4 collect the studies about wetting phenomena on rough surfaces. The physical question here is the development of an efficient numerical method to simulate the contact of a liquid drop with a possibly textured solid surface. The method should be tested against experimental observation and it should become a predictive tool useful for applications and further theoretical researches. Moreover the model behind the physics of a drop is a simplified version of those governing the shape of a biological vesicle, the archetype of a cell membrane. Therefore the techniques and the expertise derived in this work could become the starting point of new researches in this equivalently or even more interesting field.

I worked on this topic under the supervision of Prof. A. DeSimone. The results obtained are contained in the two papers [B], [C]. The first one describes the results for the 2D case and it was written also in collaboration with Prof. F. Alouges. The second one concerns 3D simulations and was written more autonomously. However, the initial collaboration with Eng. C. De Vittoria (regarding the framework of the 3D code and the solution of many programming problems) is gratefully acknowledged.

We started looking at the drawbacks of the existing solutions of the problem. The geometric formulation of the wetting problem allows for an analytic solution in the simplest situations (a water drop in air is spherical; if it is deposited on a homogeneous solid surface, it becomes a spherical cap with a characteristic contact angle). However such an achievement is no longer reachable if gravity enters or if the solid is not smooth. Even a numeric treatment of these equations would be excessively expensive and unnecessarily complicated, when possible. Leaving the concept of a mathematical surface as a boundary between water and air, other models appear. The diffuse interface model is our choice: the transition is confined in a narrow region and consequently the equations governing the system simplify and contain no singularity in case of new interfaces creation (or their destruction).

We pursued a rigorous mathematical treatment of these models, including a particular attention to the contact of the drop with the solid, which is the true innovation contained in our work from the pure mathematical point of view. Once more the construction is based on variational techniques: a $\Gamma-$convergence result to establish the link between the phase field model and the geometric one. Moreover also the algorithm employed to solve the equilibrium equations involves the gradient flow of the energy functional related to the solid-drop system.

The wetting problem is a sort of iso-perimetric problem in which we want to minimize the energy coming from the surfaces (essentially the contacts of the liquid L with the solid S and with air V) at a fixed drop volume. In the physical notation the capillary energy reads:

$$E(\omega, t) = \sigma_{SL}|\Sigma_{SL}| + \sigma_{LV}|\Sigma_{LV}| + \sigma_{SV}|\Sigma_{SV}| + \int_{\omega} U(x,t)\, d\mathcal{V}_x, \tag{3}$$

where the last term represents the effect of a body force like gravity and the coefficients σ are the surface tensions relative to the interfaces. The time dependency t accounts for evolution situations such as the one occurring in tilted plate experiments, where the solid surface on which a heavy drop rests is inclined. In this context we will consider only quasistatic evolutions.

within the phase field formulation a phase function ϕ will take the value 1 in the region occupied by the liquid and the value 0 where vapour is present. The transition layer has a width depending on a small parameter ϵ. In the limit as this value goes to zero, the original wetting problem is recovered by means of $\Gamma-$convergence. The solid appears as a boundary condition (both Dirichlet and Neumann conditions were studied) allowing for an easy treatment of complex geometries. The energy functional becomes:

$$E_\epsilon(\phi, t) = \int_{\Omega} \epsilon|\nabla\phi|^2 + \frac{1}{\epsilon}W(\phi) + \phi\, U(x,t)\, d\mathcal{V}_x, \tag{4}$$

where W is a double well potential penalizing values of ϕ far from the liquid or the vapour phases.

Notwithstanding the simplicity of the model, the numerical simulations following this strategy (through a suitable algorithm whose main feature is the conservation of the volume of the drop) are able to capture significant features of real experiments and to reproduce analytic solutions, when available. For example the hysteresis of the contact angle can be correctly simulated and checked against the known solution in the case of an horizontal solid and against experiments in the case of an inclined plane.

The simulation of a solid surface textured with rows of pillars is much more interesting. Even in the 2D case the simulated water drops deposited on such surfaces exhibit metastability properties similar to those known from experiments. Obviously 3D simulations are more striking, although more demanding.

The basic algorithm written for the two dimensional simulations cannot handle the 3D case, because of the dramatic growth in the number of degrees of freedom.

This forced us to implement a multigrid strategy on a parallel computing platform. This is not a pure programming problem, because the computing resources cannot be unlimited. Moreover the goal was to increase the resolution of the simulations near the interfaces (especially on the solid surface). The result is an adaptive mesh refinement scheme involving a non trivial triquadratic interpolation at the boundaries between coarse and fine grids and a reediting of the gradient flow algorithm.

The results of this approach are directly comparable to observations. The simulations of drops on an inclined plane are quantitatively in good agreement with published experimental data. While the numerical version of the evaporating drop on a sparse grid of pillars gives a rather precise replication of what M. Callies and D. Quéré realized in their laboratory.

References:

[A] Turco A., Passerone D., Cardin F.: *Tonelli principle: finite reduction and fixed energy molecular dynamics trajectories.* MMS, to appear (2008)

[B] A. Turco, F. Alouges, A. DeSimone: *Wetting on rough surfaces and contact angle hysteresis: numerical experiments based on a phase field model.* Preprint Sissa 91/2007/M

[C] A. Turco: *Adaptive Mesh Refinement applied to the Phase Field simulation of Wetting Phenomena.* Preprint Sissa 58/2008/M

Chapter 1

MOLECULAR DYNAMICS

1.1 The rare events problem

Molecular dynamics can be seen as the intermediate step between theoretical physics and experimental observations: it is the numerical simulation of the dynamics of atoms and molecules. A molecular dynamics experiment is good if the model governing it is physically correct and, at the same time, if the numerical scheme is robust enough: the results must be comparable to observations.

In this chapter we will focus on a problem that is much more delicate regarding the second issue, because the aim is to study a so called *rare event*: the transition of a system between two (meta)-stable configurations. These events are rare because, looking at the potential energy landscape, the probability of a transition decreases exponentially with the height of the separation barrier. Moreover in a system with many degrees of freedom the equipartition of the energy is another obstacle to overcome in order to catch the right ensemble which allows for the jump.

The challenge is not only speculative. Rare events are the building block of every chemical reaction and for example, enlarging the system, of the protein folding. The understanding of a process with this level of complexity is probably the main goal in the field and the starting point of a very wide range of applications, mainly but not only in medicine.

The improvement achieved in the algorithms behind the numerical simulations of these phenomena will be discussed in details. But first, we would like to frame this problem in the wider context of path sampling. It will be shown how to compute a single reactive trajectory with given extremal configurations, starting from a variational principle. Why could it be important in a world governed by fluc-

tuations and thermodynamics? As pointed out in previous studies (see, e.g., Bai and Elber [6] and references therein) two-point boundary algorithms applied to a description where all microscopic degrees of freedom are considered explicitly can become exceedingly expensive when the total time of the path becomes too large. Nevertheless, Bai and Elber point out that short time trajectories can become statistically important if one focuses on the transitional part of a reactive path from a reactant to a product. If the process is not diffusive, the very transition process is rather short, and a sampling limited to the transition part of the path can give information on the transient timescale of the process. It is in this kind of processes that two-point boundary algorithms can play their role.

The steps leading from a single trajectory to a complete sampling will not be treated. Instead we will present the result of a joint work with prof. Franco Cardin (univ. Padova) and dr. Daniele Passerone (EMPA, Zurich) [54]. We propose a new method for obtaining accurate trajectories at a fixed energy, a feature that could be used for subsequent extensions of sampling strategies. The first direct application could be envisioned in the microcanonical sampling with a modified Boltzmann criterion in order to enhance the sampling of important energy regions with low density of states (Wang-Landau method [56]). Another extension could be the field of extended Lagrangians (for example for systems in contact with a thermostat), where an extended conserved quantity (total "energy") can be defined for the whole system (e.g., solute + solvent + thermostat), and a controlled sampling as a function of this quantity could be introduced.

1.2 Classical answers

The problem can be briefly but precisely exposed in these terms: we consider a set of $\mathcal{N}$ particles interacting through a given potential V and we look for a physical path joining the basins of attraction of two of its (local) minima. The main sources of complexity are hidden in $\mathcal{N}$ and V: on the one hand all the modeling work is condensed in the choice of the degrees of freedom of the system and of the associated potential energy. On the other hand, simulating a realistic system implies a very rough and complicated potential energy landscape in a high dimensional phase space. However, if -as we do- a classical approach is preferred over a quantistic one, the form of the equations we want to solve is very simple, they are the Newton equation of motion (here we put all the masses equal to 1 for simplicity, or equivalently we

can consider them incorporated in the definition of V):

$$\frac{d^2q}{dt^2}(t) = -\nabla V(q(t)), \tag{1.1}$$

where $q(\cdot)$ is the $3\mathcal{N}$ dimensional position vector.

The standard integration algorithm in Molecular Dynamics is the Verlet one:

$$q(t+\Delta t) = q(t) + \Delta t \cdot \dot{q}(t) - \frac{\Delta t^2}{2}\nabla V(q(t)) \tag{1.2}$$

$$\dot{q}(t+\Delta t) = \dot{q}(t) - \frac{\Delta t}{2}\Big(\nabla V(q(t)) + \nabla V(q(t+\Delta t))\Big). \tag{1.3}$$

This scheme is very accurate for times comparable to the duration of the transition, it is a second order scheme both in the position and in the velocity (there are several versions of the Verlet algorithm, the one above is the *velocity Verlet* that indeed guarantees the precision of the description of $\dot{q}$). As a consequence we cannot employ it for an ab-initio sampling of the phase space hoping to observe a rare event: the trajectory would spend too much time in the basin of the minimum where it started. Nevertheless one can test any computed path against a Verlet one obtaining a validation of its accuracy: the idea is to use a variational principle that prescribes the extremal configuration of the trajectory and to check the results obtained with the Verlet path having the same initial position and an initial velocity equal to the computed one.

Standard variational principles are commonly used in MD, even if the Verlet algorithm remains the benchmark tool. Hamilton principle is in general the first choice, but the main drawback of its usual discretizations is the low accuracy in the conservation of first integrals of the trajectory, like the total energy. Passerone, Ceccarelli and Parrinello [43] proposed a modified functional designed ad hoc to overcome this problem: they added a penalty functional avoiding large deviations from the desired value of the energy. The new functional is (we follow the notation of the cited paper, notice that the letter θ is not a parameter):

$$S_\theta = \gamma\int_0^\tau L(q,\dot{q},t)\,dt + \mu\int_0^\tau (K+V-E)^2\,dt, \tag{1.4}$$

where L is the Lagrangian of the system, K is the kinetic energy and E is the desired value of the total energy. A fine tuning of the parameters γ and μ and an efficient stationarization algorithm could bring to interesting results, as they showed, including accurate predictions of the total time of the transition τ, but at an high computational cost and sometimes using extra numerical tools. Indeed the hope

of transforming a stationarization problem into a minimization one exploiting the positive definiteness of the second integral was unattained as we showed in [51].

Another classical variational principle can guarantee the conservation of the total energy without penalization terms: it is the Maupertuis functional, tested in this field for example in [27]. The Maupertuis functional reads:

$$\mathcal{M}_E(q(\cdot)) = \int_0^1 \sqrt{2(E - V(q(\tau)))\,|\dot{q}(\tau)|^2}\,d\tau. \tag{1.5}$$

The final extreme of the integral is 1, because the stationary curves of this functional represent only the support of the dynamical paths. The correct (nonlinear) time reparametrization can be obtained with the relation

$$\tau(t) = \int_0^t \sqrt{\frac{|\dot{q}(s)|^2}{2(E-V)}}\,ds. \tag{1.6}$$

In the next section our proposal, which is an alternative to Maupertuis functional, will be discussed. They shares many advantages, but Tonelli functional in our tests shows a higher robustness. Moreover, coupled with the relative finite dimensional technique, Tonelli functional can drop computational costs maintaining the same order of accuracy of a traditional stationarization.

1.3 Tonelli functional

Tonelli principle [50] appears in many papers concerning the existence of periodic solutions of Hamiltonian system. A summary of related results can be found in [5]. As far as we know, its first implementation in MD is in our work [54].

The space of admissible trajectories for this functional is:

$$\Gamma_{q_0,q_1} = \left\{ q(\cdot) \in H^1((0,1),\mathbb{R}^{3\mathcal{N}}) \colon \quad q(0) = q_0, \quad q(1) = q_1 \right\}.$$

The space H^1 is mandatory for this technique, but at the end it is possible to recover classical curves with well defined velocities and accelerations. For any fixed real value h (that will be the total energy of the system. The kinetic energy is denoted by K, the potential one by V), Tonelli functional is

$$\mathcal{T}_h(q(\cdot)) = \int_0^1 K(\dot{q}(\tau))\,d\tau \cdot \int_0^1 (h - V(q(\tau)))\,d\tau. \tag{1.7}$$

The potential can be singular, as the classical Lennard-Jones one which prevents any possible collision giving them an infinite energy, remaining on the other hand

bounded from below. In order to perform the regularity theory on the solution of the problem, V is required to be smooth under the desired value of the total energy.

A curve $q(\cdot) \in \Gamma_{q_0,q_1}$ is said to be a *critical curve* [5] for $\mathcal{T}_h(q)$ if for any vector $\delta q(\cdot)$ of the local tangent space $\Gamma_{0,0} = T_q\Gamma_{q_0,q_1}$:

$$\delta\mathcal{T}_h(q)\delta q := \frac{d}{d\lambda}\mathcal{T}_h(q + \lambda\delta q)|_{\lambda=0} = 0 \tag{1.8}$$

With this definition the following theorem can be stated.

Theorem 1.3.1. *A curve $q(\cdot) \in \Gamma_{q_0,q_1}$, such that $\mathcal{T}_h(q) > 0$, is critical for $\mathcal{T}_h$ if and only if its reparametrization $\bar{q}(\cdot)$, defined by*

$$[0, \omega^{-1}] \ni t \mapsto \bar{q}(t) := q(t\omega) \in \mathbb{R}^n \qquad (\tau = \omega t), \tag{1.9}$$

solves the Lagrange equations for $L = K - V$ with total energy $E = K + V = h$. The value of ω, involved in (1.9), is determined only by the knowledge of $q(\cdot)$ and h.

Proof: a direct computation will prove the assertion:

$$\begin{aligned}
\delta\mathcal{T}_h(q)\delta q &= \frac{d}{d\lambda}\left\{\int_0^1 K\big(\dot{q}(\tau) + \lambda\delta\dot{q}(\tau)\big)\,d\tau \cdot \int_0^1 \Big(h - V(q(\tau) + \lambda\delta q(\tau))\Big)\,d\tau\right\}\Bigg|_{\lambda=0} \\
&= \int_0^1 \nabla K(\dot{q}(\tau))\delta\dot{q}(\tau)\,d\tau \cdot \int_0^1 (h - V(q(\tau)))\,d\tau - \\
&- \int_0^1 K(\dot{q}(\tau))\,d\tau \cdot \int_0^1 \nabla V(q(\tau))\delta q(\tau)\,d\tau
\end{aligned} \tag{1.10}$$

so the curve is critical if and only if:

$$\omega^2 \int_0^1 \nabla K(\dot{q}(\tau))\delta\dot{q}(\tau)\,d\tau - \int_0^1 \nabla V(q(\tau))\delta q(\tau)\,d\tau = 0 \tag{1.11}$$

where,

$$\omega^2 := \frac{\int_0^1 (h - V(q(\tau)))\,d\tau}{\int_0^1 K(\dot{q}(\tau))\,d\tau} \tag{1.12}$$

This condition means that $q(\cdot)$ must be a solution of:

$$\omega^2 \frac{d^2q}{d\tau^2}(\tau) + \nabla V(q(\tau)) = 0 \tag{1.13}$$

The above calculation actually shows only that $q(\cdot)$ is a weak solution of this system of differential equations. But under the regularity assumption on the potential we can invoke standard theorems to claim that it is also a classical $\mathcal{C}^2$ solution. Moreover

$\mathcal{T}_h(q(\cdot)) > 0$, then the above ω^2 is a positive real number, so by performing the linear time reparametrization

$$[0, \omega^{-1}] \ni t \mapsto \tau(t) = \omega t \in [0, 1]$$

it is clear that $\bar{q}(t) = q(\omega t)$ solves the *mechanical* Lagrange equations:

$$\frac{d^2\bar{q}}{dt^2}(t) = -\nabla V(\bar{q}(t)) \tag{1.14}$$

Finally, recalling the conservation of energy for $\bar{q}$, and denoting by E the related total energy value,

$$E = \left(K(\frac{d\bar{q}}{dt}(t)) + V(\bar{q}(t)) \right) \Big|_{t=\tau\omega^{-1}} = \omega^2 K(\frac{dq}{d\tau}(\tau)) + V(q(\tau)),$$

by integration on τ:

$$\int_0^1 \big(E - V\big) d\tau = \omega^2 \int_0^1 K d\tau,$$

Thus the total energy E of the curve found is exactly the value h imposed from the beginning. □

1.4 Exact Finite Dimensional Reduction

Before showing the numerical results obtained with the Tonelli functional, another variational tool is introduced and it will work together with the former, increasing the capabilities of the algorithm. The technique is a modification of the classical Amann-Conley-Zehnder reduction [15]. Here reduction means that we are able to transform a problem defined over a (infinite dimensional) functional space into an algebraic one with a finite number of unknowns. The time reparametrisation of Tonelli functional can be incorporated in this framework. The main idea is quite simple: knowing only the first N Fourier components of the solution (i.e. solving system 1.26), with this reduction technique, it is possible to reconstruct exactly the entire series. The engine of this machinery is a contractive map defined on the queues (1.21) that gives the remaining (infinite) components of the solution as its unique fixed point.

The choice of the (truncated) Fourier series for the discretization of the problem may not be the optimal one, from the computational point of view. A trajectory described in terms of cartesian coordinates at fixed time steps, and/or in terms of splines joining them allows for more efficient numerical techniques for functional stationarization. However, the Fourier description represents for the moment the best

compromise between theoretical needs and computational costs. Indeed, the finite reduction technique -although it predicts exactly positions and velocities- involves integral properties of the function describing the trajectory (originally it involved the eigenfunctions of the differential operator employed and also recent studies [58] highlight the advantages of a Fourier decomposition). The results of the simulations described later in the paper are satisfactory, in our opinion. Notwithstanding this, we are investigating deeper the problem and this will be a preferred direction in our future work.

1.4.1 Hypothesis and preliminary considerations

The main hypothesis under which this developing theory does work, is that the potential should have an uniformly bounded Hessian. From the physical point of view, this means that we can concern with any non-linear force with the only prescription that if it diverges, it goes to infinity at most linearly. However, the relative potential is not necessary convex.

The value of ω appearing in (1.13) is, at the starting point, an unknown. Thus in the study of the lagrangian $\tilde{L} = K - \frac{V}{\omega^2}$, this value will be treated as a parameter of the problem satisfying equation (1.12) (see also (1.18) below). As before the boundary data are specified as $q(0) = q_0$ and $q(1) = q_1$, but for this procedure functions with more regularity are needed, hence the admissible space will be:

$$\Gamma' = \{q(\cdot) \in H^2((0,1), \mathbb{R}^{3\mathcal{N}}) : q(0) = q_0, \quad q(1) = q_1\}.$$

A function $q \in \Gamma'$ is in particular a function in L^2 for which a Fourier decomposition is available. Before entering in the details, it is important to notice that the regularity assumptions in the definition of Γ' and the boundary data are sufficient to assure the existence of the second derivative of q and to allow its calculation by a term by term derivation in the Fourier series. A simple choice for the representation is:

$$q(t) = q_0 + (q_1 - q_0)\, t + \sum_{n \in \mathbb{N}} a_n \sin(\pi n t) \tag{1.15}$$

This is not a traditional Fourier series, but it is a standard choice in molecular dynamics: it appeared already in Feynman book [28] and more recently it was used by Doll in different works, see for example [14, 22]. The convergence of this series to the original function in the H^2 norm is straightforward in Fourier analysis. The idea is to extend any function to an odd function in $(-1, 1)$ and then to use the standard Fourier series on it. We recall the main features of this decomposition.

- The function $q(t) - q_0 - (q_1 - q_0)\, t$ is, under the assumptions made, in H_0^2; therefore $q(0) = q_0$ and $q(1) = q_1$. This is due to the standard Sobolev embedding theorem.
- $-\sum \pi^2 n^2 a_n \sin(\pi n t)$ converges to $\ddot{q}$ in L^2, by Poincaré inequality. Indeed $q - q_{\bar{n}} := q - \left(q_0 + (q_1 - q_0)\, t + \sum_{n \leq \bar{n}} a_n \sin(\pi n t)\right)$ is a function in H_0^2 which tends to zero in L^2 as $\bar{n}$ goes to infinity with its first two derivatives.
- This last convergence result does not imply that $\ddot{q}$ is zero at the boundary, in fact here one cannot invoke any embedding theorem and so none information on the local behavior of the second derivative is available. The Fourier series converges only at almost every point (with respect to the Lebesgue measure).

1.4.2 The contraction and the algebraic system

With the proposed parametrization, putting $\phi = \sum_{n \in \mathbb{N}} a_n \sin(\pi n t)$ in (1.15) the equation for the modified Lagrangian system can be rewritten as:

$$\ddot{\phi} = -\frac{\nabla V(q)}{\omega^2} \tag{1.16}$$

Now the reduction procedure can start. Once fixed a number N, the space where $\ddot{\phi}$ lies is split in the following way: for any $\psi \in L^2((0,1), \mathbb{R}^{3\mathcal{N}})$ put

$$\mathbb{P}_N \psi(s) := \sum_{n \leq N} \psi_k \sin(\pi n s), \qquad \mathbb{Q}_N \psi(s) := \psi(s) - \mathbb{P}_N \psi(s), \tag{1.17}$$

obtaining $L^2 = \mathbb{P}_N L^2 \oplus \mathbb{Q}_N L^2$. The finite part will be called u, while v will be the infinite one. This is the announced separation between the initial part of the series (up to order N) and the infinite dimensional space of the queues. When no confusion can possibly arise, we will often call with the same name the function and the coefficients of the Fourier series. For technical and practical reasons, that will be immediately clarified, it is important also to keep the u component together with the real parameter ω: the pair $(\omega, \mathbb{P}_N \phi) \in \mathbb{R} \times \mathbb{P}_N L^2$ will be called $\bar{u}$. So, summing up, the set of unknowns is

$$(\bar{u}, v) = (\omega, u, v) \in \mathbb{R} \times \mathbb{P}_N L^2 \times \mathbb{Q}_N L^2 \tag{1.18}$$

For any fixed value of $\bar{u}$, we define the functional

$$G : \mathbb{Q}_N L^2 \longrightarrow \mathbb{Q}_N L^2 \tag{1.19}$$

$$v \longmapsto G(v) \tag{1.20}$$

where the n-th component of $G(v)$ in the sine basis is defined by

$$[G(v)]_n := \frac{1}{(\pi n)^2}\left[\frac{\nabla V\left(q_0 + (q_1 - q_0)\, t + u + v\right)}{\omega^2}\right]_n \qquad \text{for } n > N \tag{1.21}$$

Theorem 1.4.1. *There exist a value $\bar{N}$ such that the map G is a contraction between Banach spaces. Therefore it admits one and only one fixed point.*

Proof: for any function $\psi \in L^2((0,1), \mathbb{R}^{3\mathcal{N}})$ we can write:

$$\|\psi\|_{L^2} = \left(\int_0^1 |\psi(t)|^2_{\mathbb{R}^{3\mathcal{N}}}\, dt\right)^{\frac{1}{2}} = \left(\int_0^1 \sum_{i=1}^{3\mathcal{N}} \psi_i^2(t)\, dt\right)^{\frac{1}{2}} \tag{1.22}$$

$$= \left(\sum_{i=1}^{3\mathcal{N}} \int_0^1 \psi_i^2(t)\, dt\right)^{\frac{1}{2}} = \left(\sum_{i=1}^{3\mathcal{N}} \sum_{n=1}^{+\infty} \int_0^1 a_{in}^2 \sin^2(\pi n t), dt\right)^{\frac{1}{2}} \tag{1.23}$$

$$= \frac{1}{\sqrt{2}}\left(\sum_{i=1}^{3\mathcal{N}} \sum_{n=1}^{+\infty} a_{in}^2\right)^{\frac{1}{2}} \tag{1.24}$$

where $\psi_i(t) = \sum_n a_{in} \sin(\pi n t)$. Applying this result to the function G, the desired inequality can be proved. In the following calculation we write $\phi_0 = q_0 + (q_1 - q_0)t$, $C = \sup_{x \in \mathbb{R}^{3\mathcal{N}}} |\nabla^2 V(x)| < +\infty$ and we keep together the three spatial coordinates of G avoiding heavy notations. Thus:

$$\begin{aligned}
\|G(v_2) - G(v_1)\|_{L^2} &= \frac{1}{\sqrt{2}}\left(\sum_{n>N} |\,[G(v_2)]_n - [G(v_1)]_n\,|^2\right)^{1/2} \\
&= \frac{1}{\sqrt{2}}\left(\sum_{n>N} \frac{1}{(\pi n)^2}\left|\left[\frac{\nabla V(\phi_0 + u + v_2)}{\omega^2}\right]_n - \left[\frac{\nabla V(\phi_0 + u + v_1)}{\omega^2}\right]_n\right|^2\right)^{1/2} \\
&\leq \frac{1}{\pi^2 (N+1)^2 \omega^2 \sqrt{2}}\left(\sum_{n>N} |[\nabla V(\phi_0 + u + v_2) - \nabla V(\phi_0 + u + v_1)]_n|^2\right)^{1/2} \\
&\leq \frac{1}{\pi^2 (N+1)^2 \omega^2}\, \|\nabla V(\phi_0 + u + v_2) - \nabla V(\phi_0 + u + v_1)\|_{L^2} \\
&\leq \frac{C}{\pi^2 (N+1)^2 \omega^2}\, \|v_2 - v_1\|_{L^2}
\end{aligned} \tag{1.25}$$

If N is large enough, then $\alpha := \frac{C}{\pi^2 (N+1)^2 \omega^2} < 1$ and G is a contraction. By standard arguments we can deduce now the existence of a unique fixed point: $f(\bar{u}) = G(f(\bar{u})) \in \mathbb{Q}_N L^2$. An important remark is that $\bar{u} \mapsto f(\bar{u})$ is of class C^1, as it can proved with the implicit function theorem. □

With this function the variational problem can be translated into an algebraic one. In fact, now now we have only to solve the following finite dimensional system, where $u = \sum u_n = \sum a_n \sin(\pi n t)$ and $1 \leq n \leq N$:

$$\begin{cases} a_n &= \dfrac{1}{(\pi n)^2}\left[\dfrac{\nabla V(\phi_0 + u + f(\bar{u}))}{\omega^2}\right]_n \\ \\ \omega^2 &= \dfrac{\int_0^1 (h - V(\phi_0 + u + f(\bar{u})))\, d\tau}{\int_0^1 K\left(\frac{d}{dt}(\phi_0 + u + f(\bar{u}))(\tau)\right)\, d\tau} \end{cases} \tag{1.26}$$

If we are able to find a solution, the corresponding mechanical curve is easily recovered: first, the factor $(\pi n)^2$ is passed to the left hand side of each component of $(1.26)_1$ and of (1.21); then, we observe that $-(\pi n)^2 u_n$ for $1 \leq n \leq N$, and $-(\pi n)^2 f(\bar{u})_n$ for $n > N$, make up precisely the Fourier components of $\ddot{\phi}$. Finally, as desired, $\ddot{\phi} = -\frac{\nabla V(q)}{\omega^2}$ with the correct value of the parameter ω found in (1.26).

The numerical implementation of this technique requires a second cut in the Fourier series: the components from M to infinity will not be considered. A suitable algorithm to couple the finite reduction with Tonelli functional is the topic of section §1.6. For the moment we want to remark that this second cut does not interfere with the contractivity of the map G: if we call $G_{N,M}$ the map corresponding to the harmonics from $N+1$ to M, a simple extension of (1.25) shows that it is more contractive than G for any choice of M [51].

1.4.3 The reduction for the harmonic oscillator

A simple example is useful to understand the role of the parameter N in the above construction: the harmonic oscillator. The interesting point is the condition for the contraction: the theorem says that one can always take an N large enough, but if ω is too small, the value reached by the number of Fourier coefficient is out of any computational purpose.

Considering the classical harmonic oscillator of equation $\ddot{q} + kq = 0$, the contraction coefficient can be computed as follows: the period of an oscillation is $T = \frac{2\pi}{\sqrt{k}}$, the supremum of the Hessian of the potential is $C = k$, hence

$$C = \frac{(2\pi)^2}{T^2} \tag{1.27}$$

Denoting by $T_\omega = \frac{1}{\omega}$ the total time related to ω in Tonelli functional (1.9), we obtain

$$\alpha = \frac{4}{T^2(N+1)^2\omega^2} = \frac{4T_\omega^2}{T^2(N+1)^2} < 1 \tag{1.28}$$

so the contraction works if

$$N + 1 > 2\frac{T_\omega}{T} \tag{1.29}$$

In this case this estimate is sharp: if we consider a trajectory whose time length is less than half of a period T, the estimate tells that $N = 0$ is admissible and so all the Fourier coefficients can be computed with the contraction. On the other hand, if the time length is over $T/2$, at least $N = 1$ is needed. This coincides with the theory of conjugate points: exactly at half of a period the first conjugate point appears. After it the trajectory is no more a minimum for the action functional and we cannot expect that the contraction will converge with $N = 0$. From this it is possible to learn that in more complex cases we must take care about the product $\omega(N + 1)$: for any chosen value of N, there is a largest value of the trajectory total time ω^{-1} that cannot be overcome without losing the contractivity.

1.5 Performance of Tonelli principle and comparison with Maupertuis principle

Maupertuis principle $\mathcal{M}_E$ -although it is not defined over all the configuration space- offers directly a geometric formulation of the problem in terms of a Riemannian metric and its geodesics. Unfortunately this metric becomes singular whenever $V(q(\tau))$ approaches (from below) E. Moreover in these situations the precision of the parametrization decreases and this can be highlighted in any standard numerical implementation of this principle. We show this with a simple example: a one-dimensional double well.

Both principles (Tonelli and Maupertuis) are translated into algorithms with similar techniques as the ones described in [43]: the path is discretized and the functional optimization is transformed into an optimization of a discretized action, function of the internal degrees of freedom of the path (the extremes and the total energy are kept fixed). In our case we set $V(q) = 0.25 \times q^4 - 0.5 \times q^2$, with two minima at $q = \pm 1$ and a central transition state with zero potential energy. If necessary, we also use a Monte Carlo based simulated annealing with the norm of the gradient (see later eq. (1.33) for Tonelli's case; the implementation for Maupertuis principle is similar) as objective function. This procedure shows more stability with respect to conjugate residual in the case of Maupertuis principle.

We set the fixed extremes q_0 and q_1 in the two basins of the potential, and we consider as trial trajectory a linear interpolation between q_0 and q_1. As a first

test, we notice that we can find a solution with any desired positive energy using Tonelli principle, both starting from the linear interpolation and from a random perturbation of a known solution (e.g., a solution that "bounces" on the walls of the well before the transition).

In general, the same success is obtained also with Maupertuis principle, with some important exceptions. We will indeed focus on the particular cases where the total energy is very close to the barrier. All our simulations are performed with 200 intermediate slices.

In fig. 1.1 the solution of Tonelli principle (top panel, above) and the one of Maupertuis principle (top panel, below) are showed for a total energy of $E = 0.1$, using a starting path already close to the solution. The solutions on this panel correspond to a total time of $\tau = 6.67$. This total time is correct for such energy, as verified separately (using Hamilton principle).

The only difference between the two subpanels can be seen in the region where kinetic energy is small. Whereas Tonelli principle describes the whole potential profile around the maximum in an accurate manner, the time dilation inherent to the geometric trajectory leads to a poor sampling of the region around the barrier in the Maupertuis case.

If the total energy is decreased, and we start already close to the solution, both principles behave more or less in the same correct manner. When $E \simeq 10^{-4}$, the precision of Maupertuis principle is better than the one on Tonelli's: in this particular case, the resulting trajectories from Tonelli principle correspond to a total energy smaller than the prescribed value. We found empirically that the error on the total energy for the Tonelli functional is of the order of $\Delta E \simeq 8 \times 10^{-5}$. We are presently investigating the numeric origin of this systematic error.

A more serious problem is represented by the fact that Maupertuis funcional has a delicate behavior (due to the presence of the square root of the difference $E - V$) in the proximity of the barrier. An example starting from a linear trial path randomized with an amplitude $\Delta x = 0.2$ is showed here. The optimization with Tonelli principle leads to a correct trajectory with the prescribed energy of $E = 0.01$, whereas Maupertuis principle suffers from the fact that the time intervals are derived point by point in the path from the ratio between geometric kinetic energy and square root of energy difference $\sqrt{E - V(q)}$. Since the geometric kinetic energy is calculated by finite difference on a noisy trajectory, the fluctuations in the path are going out of control: the result of the failed optimization of the path is

shown in fig. 1.1, bottom panel. This failure calls for more suitable algorithms based on a multi-scale calculation of the kinetic energy; this is not needed in the case of Tonelli principle. An additional problem in the Maupertuis functional is represented by the timestep dilatations in the vicinity of the barrier. Such time dilatations are inversely proportional to $\sqrt{E - V(q)}$.

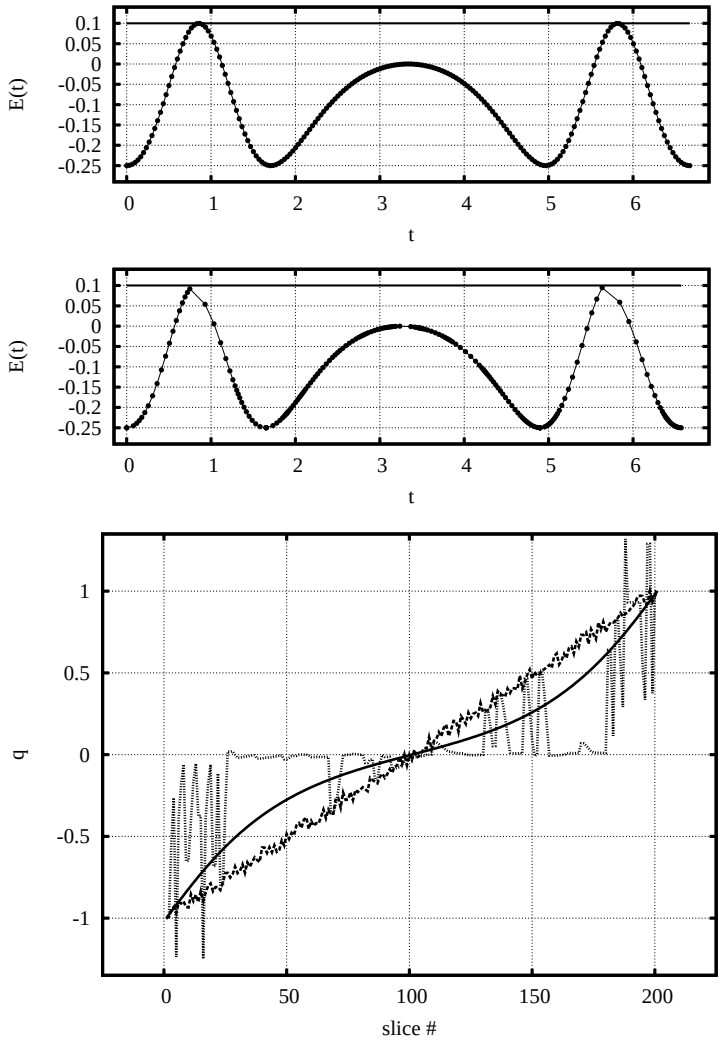

Figure 1.1: Comparison between Tonelli and Maupertuis functional in finding trajectories at total energies close to the barrier. Top panel: energies obtained from Tonelli functional, starting from good or randomized guesses, at $E = 0.1$ (above) and Maupertuis functional, starting from good or randomized guesses; bottom panel: failed Maupertuis optimization (dotted line) and Tonelli optimization (continuous line), starting from a randomized guess (dashed line), at $E = 0.01$. In this case, the coordinate as a function of path slice is shown. The total time is the correct value of $\tau = 5.59$ for the optimized Tonelli path and a exceedingly large value of $\tau = 74$ for the Maupertuis path which did not reach convergence in this case.

1.5.1 Mueller potential

We test the Tonelli functional with the widely known two-dimensional Mueller potential [40]. It is a popular test case for reaction path methods; its analytic form can be found for example in eq. 4 in Bai and Elber paper [6], and it has three minima and two main transition states.

In their paper, Bai and Elber noticed that for each total energy or total time, several different paths are possible, and that not all the energies are available for paths with a given total time.

Using Tonelli principle we show that it is possible to obtain different paths with the same energy, joining the same endpoints; moreover, we underline a difficulty of energy-based variational principles: it is not granted that local optimizers can find solutions with a requested energy. Instead, a given path basin can contain trajectories with other energies, that can be still found using Tonelli principle with another prescribed total energy.

To illustrate the first point, we first generated a relatively high energy trajectory ($E = -11.5$) using a Verlet algorithm with a timestep $\Delta t = 0.003$. Using this trajectory as starting point, we run a simulated annealing procedure using as target function the sum of squared residual errors on Tonelli's equations of motion. We use 150 intermediate slices, for a total of 300 degrees of freedom.

Depending on the simulated annealing protocol, the algorithm ends close to the original path or in another basin of attraction. A refinement using the conjugate residual method [46] leads in both cases to a solution of Tonelli principle. But as it can be seen from figure 1.2, the two solutions are different, although with the same energy.

The same exercise repeated with Maupertuis principle succeeds in finding again the original Verlet path, but not in reaching another basin of attraction and a different trajectory with the same energy.

The second attempt was to obtain a completely new path starting only from the knowledge of the extremes. First of all, we generated a trial path by interpolation of the linear interpolation between the two main minima. Starting from the straight path, we run a simulated annealing procedure using as target function the sum of squared residual errors on Tonelli equations of motion.

We set at total energy a value $E = -40$, just above the position of the main transition state. We divide our path in 50 slices, for a total of 100 degrees of freedom. After the simulated annealing procedure, we use a conjugate residual method in order

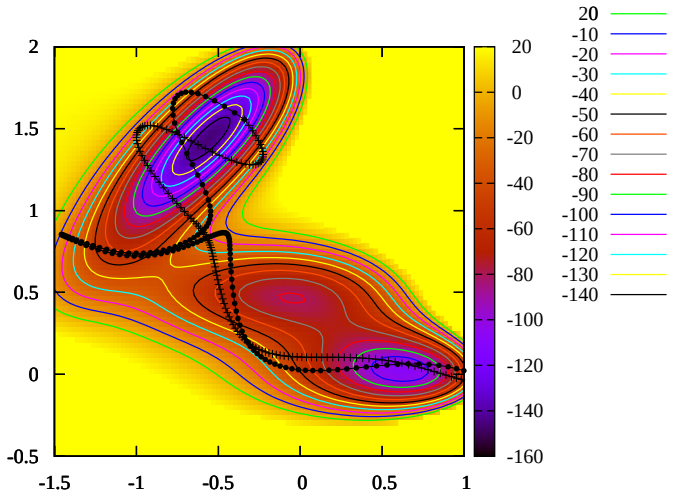

Figure 1.2: Two trajectories in the Mueller potentials, one obtained with Verlet integration (crosses), the other one (points) obtained from the former with Tonelli principle and simulated annealing. Both trajectories have an energy $E = -11.5$, and the same extremes.

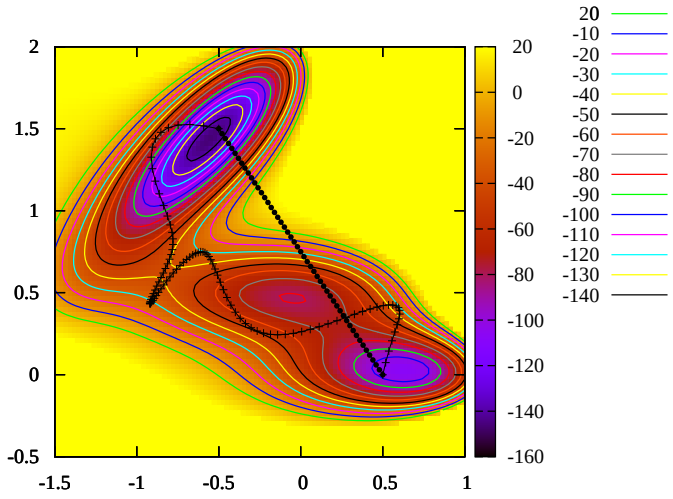

Figure 1.3: Trajectory in the Mueller potential (crosses) obtained from the linear interpolation (points), using Tonelli principle and the simulated annealing algorithm followed by a conjugate residual refinement. The trajectory has a total energy of $E = -28$.

to refine the solution. We observe that with the prescribed value of the energy, we cannot find a solution close to the outcome of the simulated annealing. Conversely,

if the conjugate residual is applied to the same starting point, but using Tonelli principle with a energy larger than a certain threshold ($E > -28$ in this case), the local optimization algorithm is able to find a solution of Tonelli principle, shown in the figure for the limiting case $E = -28$.

As a check, we apply Hamilton principle to the optimized trajectory, using a fixed total time , and we obtain the trajectory outlined in figure 1.3, which has a conserved energy of $E = -28$. The optimization using Maupertuis principle could not lead in this case to a solution of the problem, due to the already sketched difficulties related with the term $(E - V)$ in the denominator of the gradient of the functional.

1.6 An algorithm for the contraction

The advantages of the Tonelli functional can be amplified with the announced coupling with the reduction technique. An adequate algorithm is needed, because the relation between $\bar{u}$ and $f(\bar{u})$ is only implicit in the theory explained above. Our proposal can be schematized as follows:

- set q_0 and q_1, the initial and final points of the trajectory;
- find an initial path π_0 connecting q_0 and q_1. This can be a linear interpolation, or an approximation to a minimum energy path with a few intermediate images; the latter approach gives a reasonable estimate of the maximum value of the potential energy V_{max};
- discretize π_0 into M slices;
- set the total energy E at a value larger than V_{max};
- extract the finite reduction threshold N from the contraction condition (1.25) this condition requires an estimate of the supremum of the Hessian in the potential;
- *start iteration:* expand the path π_0 in Fourier series, and keep the first N harmonics. This generates the finite dimensional system (1.26), that can be solved using iterative methods like the conjugate residual [46]. In the first step, set the harmonics $N+1$ to M to zero, corresponding to setting $f(u) = 0$ in eq. (1.26). Only a few steps of conjugate residual are performed, this generates a new path $u_1 = \sum_1^N a_n \sin(\pi n t)$;

- u_1 is inserted into (1.21), which is a contraction if N was carefully chosen. That leads to a set v_1, which can be referred to as the Fourier components $N+1$ to M of the trajectory;
- the new path π_1 is found as $\pi_1 = u_1 + v_1$;
- in (1.26), set $u = u_1$, $f(u) = v_1$; the second equation in the system also provides the total time of the path;
- check whether the threshold N still leads to a contraction using the estimate (1.25);
- iterate the procedure until convergence.

1.6.1 Error estimates

A test of the quality of a generic trajectory computed with this algorithm can be performed as follows. The first step is to compute the error made by considering the truncated contraction, say $f_{N,M}(\bar{u}) = G_{N,M}(f_{N,M}(\bar{u}))$, with respect to the real one. We denote α the contractive constant in (1.25):

$$\begin{aligned}\|f_{N,M}(\bar{u}) - f(\bar{u})\| &= \|G_{N,M}(f_{N,M}(\bar{u})) - G(f(\bar{u}))\| \\ &\leq \|G_{N,M}(f_{N,M}(\bar{u})) - G_{N,M}(f(\bar{u}))\| + \|G_{N,M}(f(\bar{u})) - G(f(\bar{u}))\| \\ &\leq \alpha\|f_{N,M}(\bar{u}) - f(\bar{u})\| + \|G_{N,M}(f(\bar{u})) - G(f(\bar{u}))\|\end{aligned} \tag{1.30}$$

Hence:

$$\begin{aligned}\|f_{N,M}(\bar{u}) - f(\bar{u})\| &\leq \frac{1}{1-\alpha}\|G_{N,M}(f(\bar{u})) - G(f(\bar{u}))\| \\ &= \frac{1}{1-\alpha}\|\mathbb{Q}_M G(f(\bar{u}))\| = \frac{1}{1-\alpha}\|\mathbb{Q}_M f(\bar{u})\|\end{aligned} \tag{1.31}$$

With this information, calling q the real trajectory, $\tilde{q}$ a curve with M Fourier components (that is stationary for the M-discretized Tonelli functional) and $\bar{q}$ a curve obtained with our procedure we obtain:

$$\|q - \bar{q}\| = \|q - \tilde{q} + \tilde{q} - \bar{q}\| \leq \frac{2-\alpha}{1-\alpha}\|q - \tilde{q}\| \tag{1.32}$$

This means that we can obtain an error with the same order of magnitude of the traditional stationarization, but following a more efficient and quicker path. Numerical evidence of this are presented in the next section.

1.6.2 Oscillations of a 4-atom Lennard-Jones cluster

Here we will present a simple system on which we tested the algorithm. At the same time we take advantage of this to explain in details the implementation. The system is a concrete one (a cluster of four atoms interacting through a Lennard-Jones potential), but it is not interesting for its features: we do not want to overlap difficulties arising from the algorithm with the intrinsic problems of a more complicated (and interesting) system, that will be discussed later.

The trajectory we want to reproduce is a short oscillation of four atoms (that could model a small argon cluster). The path of a classical Verlet simulation (in the initial value representation) is drawn in figure 1.4 (for one coordinate), and the total time is $\tau = 2$ in Lennard-Jones units.

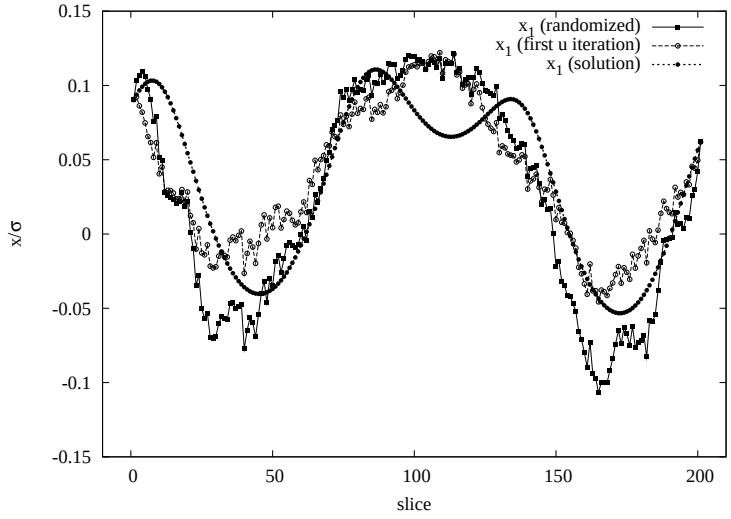

Figure 1.4: The coordinate x of atom 1 (final solution, randomized, after the first u-iteration)

In order to test the contraction strategy, we set the two extremes of this trajectory, and we perturb the trajectory. That is, we change the trajectory randomly keeping the extremes fixed. Not only, but we also apply a randomization to the u and v components. The trajectory after randomization is shown (for the same coordinate as before) in figure 1.4. Larger randomizations in such a small total time could be hard to recover. A datum not present in the picture is that, after the randomization, the total time has increased to $\tau = 12$ in Lennard-Jones units.

Now we set an N to divide the u components and the v components. In this case as an illustration we use $N = 30$. First of all, we apply an algorithm to the u components, for lowering a bit the potential energy. This is done by inverting the

sign of the potential energy. Then we set the total energy to the -4.49 value of the original trajectory. We apply the equations of Tonelli for the u for 10 iterations. We obtained a set of u that, together with the set of v coming from the randomization, give the trajectory in figure 1.4. Here the total time is 4 times the correct one.

Then we apply the contraction to the v. This contraction is applied in presence of a u that is not yet the correct solution. Nevertheless, we must obtain a fixed point.

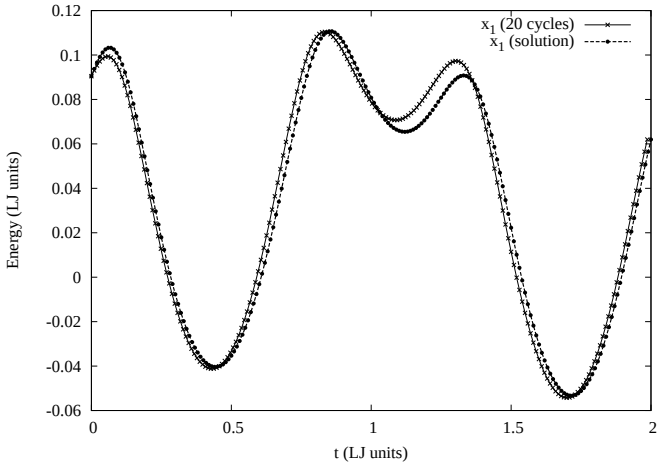

Figure 1.5: The coordinate x of atom 1 (final solution and after 20 cycles of u-optimization/contraction)

The interesting thing is that already after this first iteration, the error on the highest harmonics has decreased considerably.

We repeat the same procedure of optimization for u and the contraction, iteratively, and we succeed in optimizing the trajectory. After 3 cycles of (30 cycles of u optimization + contraction) we reach the energies (potential and total), and the error on the highest harmonics plotted on figure 1.6 and 1.7. At that point the situation has improved, and even more after twenty of such cycles. The whole series of cycles take less than 3 minutes on a normal laptop: it is a small system indeed. The final result is shown in figures 1.5 (for the x coordinate of atom 1) and 1.7 (for total and potential energies).

The trajectory is very close to the correct one. The error on the trajectory (the norm of the errors on Newton equations along the path) has decreased by several orders of magnitude throughout the procedure. The total energy, computed from derivation of the Fourier series, average to the value requested by Tonelli principle, by construction. The oscillations are due to the kinetic energy, since very small displacements in the coordinates can produce large oscillations in the kinetic energy.

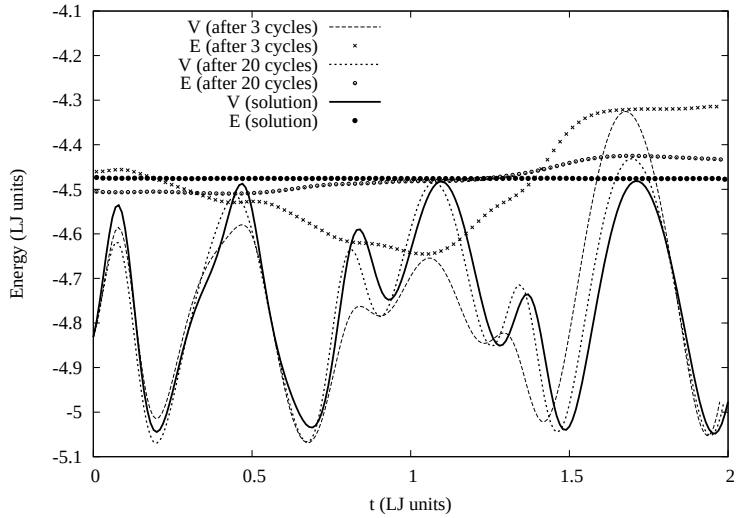

Figure 1.6: Potential and total energy for the total trajectory after 3 and 20 cycles of finite reduction, compared with the exact solution.

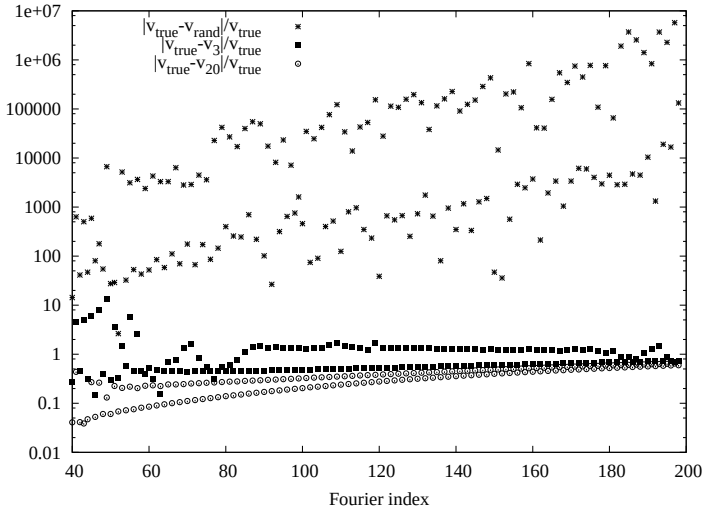

Figure 1.7: Error on the higher harmonics for the x coordinate of atom 1, after randomization, 3 cycles, and 20 cycles of finite reduction.

1.6.3 The isomerization of a 38-atom Lennard-Jones cluster

A far more demanding case is the isomerization of a 38 atom Lennard-Jones (LJ) cluster. This system is a traditional benchmark both for algorithms aiming at minima localization in a potential energy surface (PES) and for methods for extracting statistical quantities using path sampling. The PES of this system has moreover a double funnel structure, which can be seen as a "toy model" for the protein folding scenario. Recently, Bai and Elber have developed a novel strategy for sampling very

short dynamical paths [6]. In that paper, they discuss the importance of short time trajectories in the frame of path sampling. As discussed in section §1.1, an algorithm that allows to obtain trajectories at a given energy could also be of importance in a sampling procedure including the total energy as external parameter. In the Wang-Landau method [56], for example, where the sampling is enhanced in energy regions that are infrequently visited in a traditional Monte-Carlo method. Bai and Elber

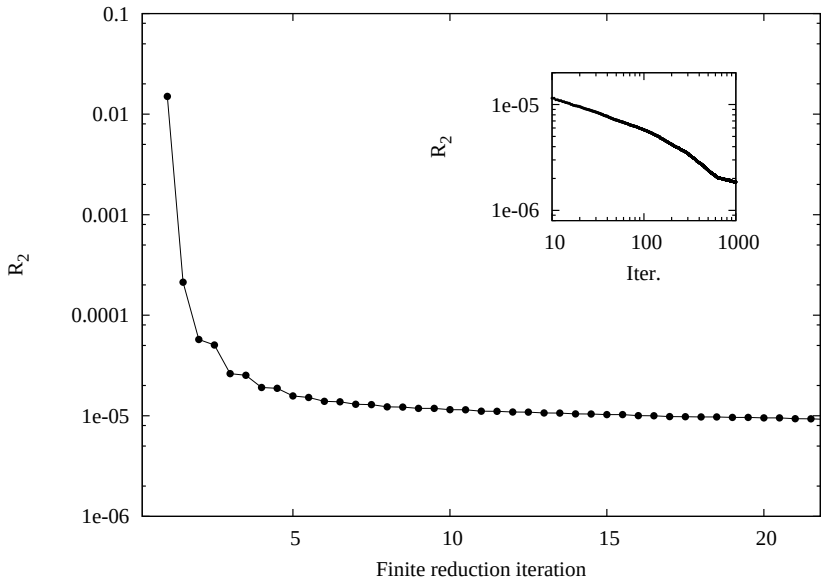

Figure 1.8: The convergence of the squared residual R_2 for the path at $E = -110$ during the finite reduction iteration. Starting from the final value obtained from simulated annealing for the 32 slice path, the residual rapidly decreases and slowly reached the value $R_2 = 0.2 \cdot 10^{-5}$ (see inset).

consider different test cases for their algorithms. For systems with few degrees of freedom (like the Mueller potential) they show in their paper the efficiency of a particular refining procedure based upon the knowledge of the Hessian matrix (Kaczmark iterations). This procedure, however, has a sizeable computational cost, and as soon as a larger system is concerned, the authors do not apply it there. Bai and Elber are able to find reactive trajectories (although with a limited number of intermediate points) for a fascinating and realistic system: they apply their method to the fast transitions between a face-centered cubic and an icosahedral structure in a solid cluster made by Argon atoms. This system can be modeled by a pairwise Lennard-Jones potential, with parameters $\sigma = \varepsilon = 1$. The authors use a standard algorithm, a simulated annealing procedure and obtain trajectories with different total times (and 32 slices), starting from a linear interpolation between the two absolute minima of the potential energy surface (fcc and icosahedral).

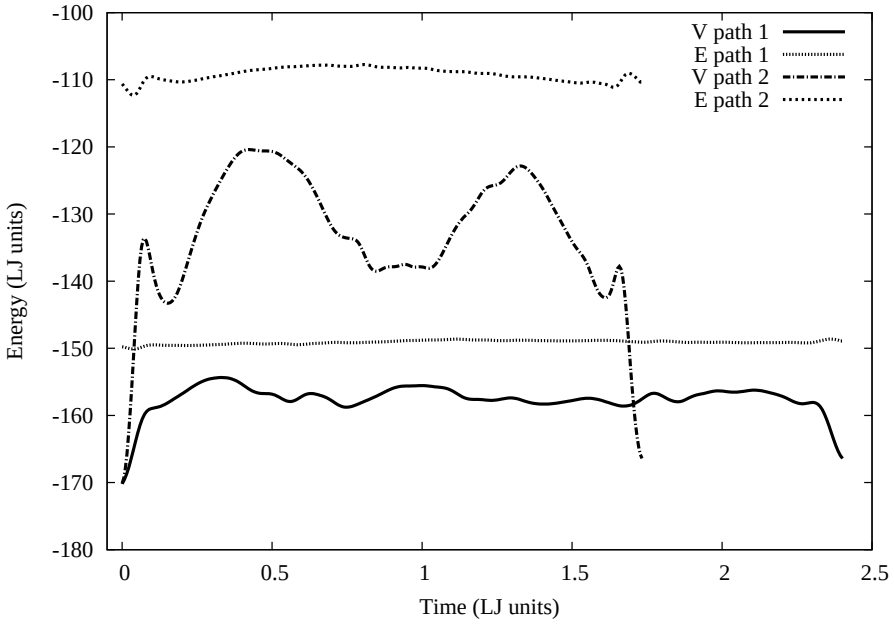

Figure 1.9: Potential and total energies for the paths at fixed total energies $E_f = -110$ and $E_f = -150$, after finite reduction with $M = 320$ total number of harmonics.

Our most demanding test is inspired from this numerical experiment (with some modifications in the optimization protocol). First of all, our starting point is an approximation to the minimum energy path (MEP), obtained by applying Tonelli principle with a "total energy" which is lower than all the potential energies of the system (it is a computational artifact to obtain a trajectory with inverted sign potential, see the discussion in [30]). The energy of the two minima is -174 (LJ units), whereas the transition state is at about -158. By comparison, the lowest energy path between the two basins, obtained with eigenvector following by Doye and coworkers [24], has an height of -169.7. Here, we are only interested in a good starting point for our procedure. Starting from this low energy path, we adopt a simulated annealing procedure as in [6] using as target function the sum on the squared residual R_2 of the equations of motion:

$$R_2 = \sum_{l=1}^{M-1} \left(q_{l+1} + q_{l-1} - 2q_l + m^{-1}\Delta^2 \frac{\partial V}{\partial q_l} \right)^2 \tag{1.33}$$

(with obvious extension to the multidimensional case) where M is the number of time slices and $\Delta = T_\omega / M$. In order to find two different paths we run two different simulated annealing protocols, setting the total energy to $E_f = -150$ and to $E_f = -110$, respectively. At each Metropolis step we recalculate the total time T_ω using eq. (1.12). During the minimization of the residuals, the average total energy

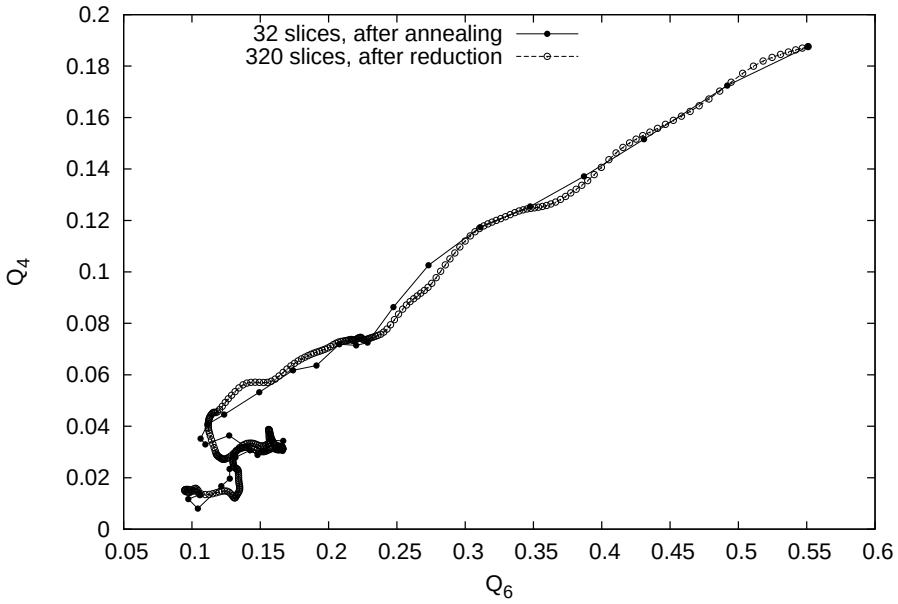

Figure 1.10: Comparison between the orientational order parameters [24] for the coarse trajectory obtained after annealing (32 slices at $E_f = -150$) and the subsequent finite reduction with iterations at the same energy.

remains fixed at E_f , as it can be easily derived from the form of Tonelli functional. After simulated annealing, our 32 slices trajectories has a residual of 0.01 and 0.004, respectively. The total energy is well conserved in both cases, and the total time is $\tau = 2.4$ and $\tau = 1.5$ in the two cases.

Exploiting the finite reduction procedure, we increase the number of slices. We start from a linear interpolation of the 32 slices, and we get a path with 320 slices. With the goal of setting a threshold for the reduction procedure (N in eq. (1.17)), we estimate the factor C in eq. (1.25). In order to avoid divergences in the second derivatives, we modify the LJ potential in unphysical regions, i.e. for $r < 0.85$ we flatten the potential toward a constant value. We verify that our trajectories never visit such regions of the PES where the $r_{ij} < 0.9$ for any pair of atoms (i, j). With this choice of the potential, eq. (1.25) gives an estimate $N = 27$. This is only an upper limit above which any contraction will be stable. Indeed, we verify that already for $N = 21$ the map is contractive. This allows us to solve iteratively the Fourier problem for the first 20 harmonics, and to treat the harmonics from $N + 1$ to $M = 320$ as a contraction.

The optimization of the first N harmonics is performed using conjugated residual method [43, 46], that is however tailored for sparse matrices, therefore not suited for

a Fourier component optimization, thus affecting the efficiency of this step. After 5 steps of conjugate residual, the contraction procedure is started, and the fastest harmonics obtained from eq. (1.21) with a very fast iterative self consistent procedure.

Successive iterations of this procedure brings the total energy to an almost perfect conservation and the residual R_2 on the equations of motion to a value of $R \simeq 10^{-5}$ within a few steps (fig. 1.8). Since the conjugate residual is not an efficient procedure in this case, further improvement of the residual are rather slow (inset of fig. 1.8) and we reach the value $R_2 = 0.2 \cdot 10^{-5}$ in about 1000 iterations. To give an idea about efficiency, a single iteration of reduction with $N = 25$ and $M = 320$ has the cost of 10 Monte Carlo sweeps with 32 slices in the former annealing procedure (one sweep corresponds to an attempted move for each coordinate along the trajectory, i.e. 31×114 energy and force evaluations)..

Figure 1.9 shows the potential and total energies of the final trajectories at $E_f = -110$ and $E_f = -150$. In figure 1.10 we show instead the fourfold and sixfold order parameter [24] along the path, for the first solution ($E_f = -150$) compared with the ones on the 32 slices path after the simulated annealing.

In order to improve further the residual R_2, we have to check periodically the assigned total energy, and to adjust it by a quantity within one percent. This behavior is probably due to the errors in the discretization and to the different definitions of the kinetic energies in the cartesian and in the Fourier representation.

As a final check, we set as initial values the coordinates at halfway along the paths, and integrate back and forth the equations of motion using the Verlet algorithm. For both cases ($E_f = -150$ and $E_f = -110$) the initial and the final basin are reached, obtaining a root mean square deviation of the Verlet trajectory from the optimized path of 0.06/atom/slice.

1.7 Conclusions and perspectives

Two are the main results of the work done. First of all, Tonelli principle has been introduced and applied, for the first time to our knowledge, to realistic systems with several degrees of freedom. Maupertuis principle has many interesting features, because it provides a Riemannian metric and it allows for a local adaptivity of the time reparametrization. Otherwise Tonelli, with its stability properties and easy implementation, is an interesting alternative. We believe that the new introduced

functional leads to a cleaner strategy because standard algorithms can be used even in situations where $\mathcal{M}_E$ shows problems. In future works it would be worth to exploit its application to complex problems.

Moreover, a well defined reduction strategy has been presented which allows the successive inclusion of faster harmonics in the path. In this scheme the tail of the Fourier series is treated as a computationally convenient contraction. The procedure has been applied to examples of increasing complexity, including a 38 atom Lennard-Jones cluster, for which two trajectories discretized into 320 time slices, and two different preassigned total energies were found.

The biggest improvement in the algorithms should concern the optimization of the slow harmonics, since the present conjugate residual method does not appear to be efficient in Fourier representation. This problem is the first we would like to solve in future refinements of the technique.

It is clear that the initial value representation of molecular dynamics, although plagued by the well-known chaotic behavior [42], is computationally extremely convenient, and remains therefore the cornerstone of popular strategies such as path sampling [10]. However, the combination of Tonelli principle together with the finite reduction should help in bridging the gap between initial value and two-point boundary representations in the field of rare events, not to mention the fact that the latter representations allows to obtain a detailed dynamical trajectory, at a given energy (even just above a barrier), joining two fixed points in the configuration space.

Chapter 2

WETTING: physical scenario and mathematical models

2.1 The geometric approach

We start the description of wetting phenomena with the derivation of the shape equations for a liquid drop deposited on a solid surface. We suppose it subjected to surface tensions and gravitational field (or a more general body force). The solid surface is first considered smooth. In a second step we will consider the case of a continuous but not smooth solid. The model is variational, following [29] we construct the total energy of the system and the desired equations are the Euler-Lagrange conditions granting that the energy is stationary. This is the so called geometric approach to the problem, because the interface between the liquid and the surrounding fluid (usually air) is represented by a $2D$ surface. Therefore it is correctly described in terms of differential geometry. In the next section we recall the main basic notions about the theory of embedded real surfaces in order to establish notations and to facilitate the reading of the sequel.

2.1.1 Preliminars

A surface is a subset of $\mathbb{R}^3$ defined by its peculiar properties; more precisely $S \subseteq \mathbb{R}^3$ is a *regular surface* [18] if for any point $p \in S$ there exist a neighborhood $V \subset \mathbb{R}^3$ and a map $\mathbf{x} : U \to V \cap S$, where $U \subset \mathbb{R}^2$ such that:

- $\mathbf{x}(u, v) \in \mathcal{C}^\infty$,
- $\mathbf{x}$ is an homeomorphism,

- for all $q \in U$, $d\mathbf{x}_q : \mathbb{R}^2 \to \mathbb{R}^3$ is one-to-one.

Other definitions are possible. A *parametrized surface* is a differentiable map $\mathbf{x} : U \subset \mathbb{R}^2 \to \mathbb{R}^3$, the set $\mathbf{x}(U)$ is called the trace of $\mathbf{x}$ and the surface is said to be regular if $d\mathbf{x}_q$ is one-to-one for any $q \in U$. Another possibility is to call a surface a two dimensional manifold, where a $\mathcal{C}^\infty$ *manifold* is a pair $(\mathcal{M}, \mathcal{F})$. Here $\mathcal{M}$ is a second countable locally Euclidean space and $\mathcal{F}$ is a differentiable structure: $\mathcal{F} = \{(U_\alpha, \phi_\alpha), \alpha \in I\}$, $\bigcup_{\alpha\in I} U_\alpha = \mathcal{M}$, $\phi_\alpha \circ \phi_\beta^{-1} \in \mathcal{C}^\infty$ with the condition that the collection has to be maximal. However, working with the first definition, the concept of *change of parameters* is naturally introduced.

Theorem 2.1.1. *Let $p \in S$ and let $\mathbf{x} : U \subset \mathbb{R}^2 \to S$ and $\mathbf{y} : V \subset \mathbb{R}^2 \to S$ be two parameterizations of S such that $p \in \mathbf{x}(U) \cap \mathbf{y}(V) = W$. Then the function $h = \mathbf{x}^{-1} \circ \mathbf{y} : \mathbf{y}^{-1}(W) \to \mathbf{x}^{-1}(W)$ is a diffeomorphism and it is called a change of parameters.*

Proof: clearly h is an homeomorphism, now let $r \in \mathbf{y}^{-1}(W)$ and $q = h(r)$. Without loss of generality the map $\mathbf{x}$ can be thought as satisfying $\frac{\partial(x,y)}{\partial(u,v)}(q) \neq 0$. Define $F : U \times \mathbb{R} \to \mathbb{R}^3$ as $F(u, v, t) = (x(u, v), y(u, v), z(u, v) + t)$, where here and before the functions x, y, z are the components of the map $\mathbf{x}$. The function F is differentiable, $F_{|_{U\times\{0\}}} = \mathbf{x}$ and the assumption guarantees that $|dF_q| = \frac{\partial(x,y)}{\partial(u,v)}(q) \neq 0$. The implicit function theorem states the existence of a neighborhood $M \ni \mathbf{x}(q)$ where F^{-1} is defined as a $\mathcal{C}^\infty$ function. By continuity of $\mathbf{y}$ there exists $r \in N \subset V$ with $\mathbf{y}(N) \subset M$ and $h_{|_N} = F^{-1} \circ \mathbf{y}_{|_N}$. Thus h is a diffeomorphism at r. □

A function $f : V \subset S \to \mathbb{R}$ is differentiable at p if $\exists \mathbf{x} : U \subset \mathbb{R}^2 \to S$, $p \in \mathbf{x}(U)$ such that $f \circ \mathbf{x}$ is differentiable at $\mathbf{x}^{-1}(p)$. If f is differentiable in a parametrization, then it is so in any other, by the theorem just proved: $f \circ \mathbf{y} = f \circ \mathbf{x} \circ h$.

The *tangent space* to S at p coincides for all the possible parameterizations with $d\mathbf{x}_q(\mathbb{R}^2)$. The canonical basis is $\langle \mathbf{x}_u, \mathbf{x}_v \rangle$, where $\mathbf{x}_u = \frac{\partial \mathbf{x}}{\partial u}$ and $\mathbf{x}_v = \frac{\partial \mathbf{x}}{\partial v}$.

The *differential* of $\phi : V \subset S_1 \to S_2$ at p is the linear map $d\phi_p : T_pS_1 \to T_{\phi(p)}S_2$ defined as: $d\phi_p(w) = \beta'(0)$ where $w = \alpha'(0)$, $\alpha : (-\epsilon, \epsilon) \to V$, $\alpha(0) = p$, $\beta = \phi \circ \alpha$. If $\alpha(t) := (u(t), v(t))$ and $\phi(u, v) := (\phi_1(u, v), \phi_2(u, v))$, then $\beta(t) =$

$(\phi_1(u(t), v(t)), \phi_2(u(t), v(t))$ and:

$$\beta'(0) = d\phi_p(w) = \begin{pmatrix} \frac{\partial \phi_1}{\partial u} & \frac{\partial \phi_1}{\partial v} \\ \\ \frac{\partial \phi_2}{\partial u} & \frac{\partial \phi_2}{\partial v} \end{pmatrix} \begin{pmatrix} u'(0) \\ \\ v'(0) \end{pmatrix}. \tag{2.1}$$

The *first fundamental form* is a quadratic form $I_p(w) = \langle w, w \rangle$, where $w \in T_pS$ and $\langle \cdot, \cdot \rangle$ is the inner product in $\mathbb{R}^3$. More precisely every T_pS inherits the interior product of $\mathbb{R}^3$ and a good notation is $\langle \cdot, \cdot \rangle_p$ recalling that it lives in T_pS.

In terms of the basis of T_pS the form becomes:

$$\begin{aligned} I_p(w) &= I_p(\alpha'(0)) = \langle \alpha'(0), \alpha'(0) \rangle_p = \\ &= \langle \mathbf{x}_u u' + \mathbf{x}_v v', \mathbf{x}_u u' + \mathbf{x}_v v' \rangle_p = \\ &= \langle \mathbf{x}_u, \mathbf{x}_u \rangle_p (u')^2 + 2\langle \mathbf{x}_u, \mathbf{x}_v \rangle_p u'v' + \langle \mathbf{x}_v, \mathbf{x}_v \rangle_p (v')^2 \\ &= E(u')^2 + 2Fu'v' + G(v')^2 \end{aligned} \tag{2.2}$$

Introducing a change of parameters, the first fundamental form does not change its value and also maintains its structure, obviously with the coefficients relative to the new basis. The first fundamental form I_p enters in measurement on the surface, for example:

$$s(t) = \int_0^t \sqrt{I(\alpha'(\tau))}\, d\tau \tag{2.3}$$

is the arc length of a parametrized curve $\alpha(\cdot)$ and

$$\cos\phi = \frac{\langle \mathbf{x}_u, \mathbf{x}_v \rangle}{|\mathbf{x}_u||\mathbf{x}_v|} = \frac{F}{\sqrt{EG}} \tag{2.4}$$

gives the angle between the coordinate curves.

The *area* of a bounded region $R \subset S$ is given by

$$A(R) = \iint_Q |\mathbf{x}_u \wedge \mathbf{x}_v|\, dudv, \tag{2.5}$$

where $Q = \mathbf{x}^{-1}(R)$. It is useful to notice that $|\mathbf{x}_u \wedge \mathbf{x}_v|^2 + \langle \mathbf{x}_u, \mathbf{x}_v \rangle^2 = |\mathbf{x}_u|^2 |\mathbf{x}_v|^2$ and hence:

$$|\mathbf{x}_u \wedge \mathbf{x}_v| = \sqrt{EG - F^2}. \tag{2.6}$$

The *unit normal* vector at p is $N = \frac{\mathbf{x}_u \wedge \mathbf{x}_v}{|\mathbf{x}_u \wedge \mathbf{x}_v|}(p)$. And the map $N : S \to \mathcal{S}^2$, $p \mapsto N(p)$ is called the *Gauss map*. This map is differentiable $dN_p : T_pS \to T_{N(p)}\mathcal{S}^2$.

Notice that these planes are parallel, therefore dN_p can be seen as a map on T_pS: $dN_p(w) = \frac{d}{dt}(N \circ \alpha(t))|_{t=0}$, with $\alpha(0) = p$, $\alpha'(0) = w$.

The *second fundamental form* is a quadratic form given by $II_p(v) = -\langle dN_p(v), v\rangle$, where $v \in T_pS$. Given a regular curve C on S passing through p, the *normal curvature* of C is $k_n = k\cos\theta$; where k is the curvature of C at p, $\cos\theta = \langle n, N\rangle$, n is the normal vector to C, N is the normal vector to S at p.

Choosing a suitable basis it is possible to write $dN_p(e_i) = k_i e_i$ for $i = 1, 2$. The *principal curvatures* are defined at p as the eigenvalues of this quadratic form. The maximum value of normal curvature will be denoted as k_1 and the minimum k_2.

The determinant of dN_p is the *Gaussian* curvature K at p. The negative of half of the trace of dN_p is the *mean* curvature H. By the invariance properties of these functions, they can be computed easily as $K = k_1k_2$ and $H = (k_1 + k_2)/2$. However, another useful formula for the mean curvature is:

$$2H = \frac{Eg - 2Ff + Ge}{EG - F^2}, \tag{2.7}$$

where $e = -\langle \mathbf{x}_u, N_u\rangle$, $2f = (\langle \mathbf{x}_u, N_v\rangle + \langle \mathbf{x}_v, N_u\rangle)$, and $g = -\langle \mathbf{x}_v, N_v\rangle$.

2.1.2 Shape equations

We present here the derivation for Laplace (2.9) and Young (2.10) laws elaborated originally by Gauss and rewrote by Finn in [29], where it is possible to find also some historical notes.

The system under consideration is a three-phase system in which an incompressible liquid, a gas and a solid coexist (the case of two immiscible fluids and a solid can be treated in the same way). The unknown surface dividing the two fluids is called $\mathcal{S}$. The position of the solid is supposed to be fixed and its surface can be split into $\mathcal{S}^*$, the wetted part, and $\hat{\mathcal{S}}^*$, the part in contact with gas.

The total energy of the system is the sum of four terms:

$$\mathcal{E} = \sigma\mathcal{S} - \sigma\beta\mathcal{S}^* + \int U\rho\, dx + \sigma\lambda\mathcal{V} \tag{2.8}$$

The first term is the surface energy related to the liquid-air interface (here $\mathcal{S}$ stands for the area of $\mathcal{S}$. The same applies to $\mathcal{S}^*$). The meaning of this term is that liquid particles must feel an attraction among them in order to maintain the separation of

the two fluids. The force is proportional to the surface area and the coefficient σ is the *surface tension*, whose dimension is that of a force per unit length. The second term is similar to the first, but it describes the interactions of the fluids with the solid. Since the sum of the wet and dry part is constant (for any movement of the liquid), various parametrization of this term are possible: here we prefer this formulation in which σ can be factorized out, later we will use the classical identification of the surface tensions related to the three possible interfaces σ_{SL}, σ_{SV}, σ_{LV}.

The third term represents the gravitational energy. The function U is a potential energy per unit mass depending on the position inside the drop. The density ρ can be taken equal to zero outside the liquid and therefore the domain of integration can be restricted to a volume containing any possible variation of the surface $\mathcal{S}$.

Finally, the last term is related to the requested volume constraint: it is imposed through a Lagrange multiplier λ to be determined (the factor σ is included here only for simplicity).

Theorem 2.1.2. *The conditions for the capillary energy* (2.8) *to be stationary, under suitable variation of* $\mathcal{S}$*, are:*

$$2H = \lambda + \frac{1}{\sigma} U\rho, \tag{2.9}$$

where H *is the mean curvature of the surface* $\mathcal{S}$*, and*

$$\cos\gamma = \beta, \tag{2.10}$$

in which γ *is the* contact angle*, the angle between the liquid and the solid, measured on a normal plane starting from inside the drop.*

Proof: the admissible variations are normal variations (far from the liquid-solid contact line), but we require the preservation of the contact between $\mathcal{S}$ and the solid surface. More precisely, the varied surface in local coordinates will be:

$$\mathcal{S}(\epsilon) = \mathbf{x}(\alpha, \beta) + \epsilon\left[\xi\mathbf{N} + \eta\mathbf{T}\right] + O(\epsilon^2). \tag{2.11}$$

The parametrization $\mathbf{x}(\alpha, \beta)$ refers to the unvaried surface, that will be denoted as $\mathcal{S}_0$. The variation vector, briefly denoted with $\epsilon\zeta$ when needed, is composed of a normal and a tangential part. The vector $\mathbf{N}$ is the unit normal on $\mathcal{S}$, directed outside the drop. The vector $\mathbf{T}$, tangent to $\mathcal{S}$, is defined only in a neighborhood of the contact line Σ between the liquid and the solid. This strip will be called Σ_δ to denote its width. The vector $\mathbf{T}$ is needed in order to assure the contact of the varied

surface with the solid, and therefore it has to be orthogonal to Σ, for the points living on it, and directed towards the solid.

The values of ξ and η are arbitrary, but they must satisfies three conditions. The variation must be small and controlled by ϵ, thus it is necessary that $\xi^2+\eta^2 \leq 1$. As we said before the tangential part is limited on a strip, hence $\operatorname{supp}\eta \subset \Sigma_\delta$. Finally, the direction allowed on the solid is the tangential one, so $\xi\mathbf{N}+\eta\mathbf{T}$ must be tangent to $\mathcal{S}^*$ on Σ. Under these assumptions it can be proved that an $O(\epsilon^2)$ term is enough to maintain the boundary of $\mathcal{S}$ on the solid surface.

Recalling formula (2.5) for the area of a surface, the derivative of the varied area can be computed:

$$\dot{\mathcal{S}} := \left.\frac{\partial \mathcal{S}}{\partial \epsilon}\right|_{\epsilon=0} = \int \frac{E_0\langle \mathbf{x}_\beta, \zeta_\beta\rangle - F_0(\langle \mathbf{x}_\alpha, \zeta_\beta\rangle + \langle \mathbf{x}_\beta, \zeta_\alpha\rangle) + G_0\langle \mathbf{x}_\alpha, \zeta_\alpha\rangle}{W_0}\, d\alpha d\beta, \quad (2.12)$$

where $W_0 = \sqrt{E_0G_0 - F_0^2}$. Further uninteresting manipulations of the right hand side (including an integration by parts, the usage of formula (2.7) and the identity $\triangle\mathbf{x} = 2H\mathbf{N}$, [36]) leads to the simplification:

$$\dot{\mathcal{S}} = -2\int_{\mathcal{S}} \xi H d\mathcal{S} + \oint_\Sigma \eta\, ds \quad (2.13)$$

For the corresponding calculation regarding $\mathcal{S}^*$, an important role is played by the unit exterior normal to Σ in the tangent plane of $\mathcal{S}^*$, say ν. Since $\langle \mathbf{N}, \nu\rangle = \sin\gamma$ and $\langle \mathbf{T}, \nu\rangle = \cos\gamma$, the result is:

$$\dot{\mathcal{S}}^* = \oint_\Sigma \langle (\xi\mathbf{N}+\eta\mathbf{T}), \nu\rangle\, ds = \oint_\Sigma (\xi\sin\gamma + \eta\cos\gamma)\, ds \quad (2.14)$$

The variation for the volume and gravitational terms are obtained considering the fact that the changes in volume due to $\mathbf{T}$ are negligible with respect to those related to $\mathbf{N}$. More precisely:

$$\mathcal{V}(\epsilon) - \mathcal{V}_0 = \epsilon \int_{\mathcal{S}\setminus\Sigma_\delta} \xi\, d\mathcal{S} + O(\epsilon^2) + \mathcal{V}_\delta, \quad (2.15)$$

where $\mathcal{V}_\delta$ is the change in volume related to the movement under $\epsilon\zeta$ of Σ_δ. The condition on the variation gives the estimate $\mathcal{V}_\delta < C\epsilon(\epsilon+\delta)|\Sigma|$. Similarly one can obtain

$$\int_{\mathcal{V}(\epsilon)} U\rho\, dx - \int_{\mathcal{V}_0} U\rho\, dx = \epsilon \int_{\mathcal{S}\setminus\Sigma_\delta} \xi U\rho\, d\mathcal{S} + O(\epsilon^2) + W_\delta, \quad (2.16)$$

with the bound $W_\delta < CM\epsilon(\epsilon+\delta)|\Sigma|$. Here M is the maximum value of $|V\rho|$ in a suitable tubular domain around Σ_δ. Dividing by ϵ, taking the limit as ϵ goes to zero

and adding the previous terms, the first variation of the energy is obtained:

$$\dot{\mathcal{E}} = \int_{\mathcal{S}} \xi \left(-2H + \frac{1}{\sigma} U\rho + \lambda \right) d\mathcal{S} + \oint_{\Sigma} \left[-\beta\xi \sin\gamma + \eta(1 - \beta\cos\gamma) \right] ds \qquad (2.17)$$

Consider now a variation with $\eta \equiv 0$, ξ positive and with support shrinking to a point of $\mathcal{S}$: the energy is stationary if and only if the first integral is zero regardless of ξ, exactly like in (2.9). If now we choose $\xi = \tau \sin\gamma$ and $\eta = \tau\cos\gamma$, a similar argument proves the second part of the theorem. □

2.1.3 Condition at a corner

We consider now the situation of a corner in the solid surface. For simplicity we treat only the case of two half planes joined by their generating line. The symmetries of this choice imply that locally the situation is equivalent to a 2D formulation.

Suppose that, for example, the right end of $\mathcal{S}_0$ touches the solid exactly on the corner (otherwise the first variation would not see the angle). Equilibrium conditions are obtained considering unilateral variations of the liquid-air interface. The idea is that the direction in which the triple junction point (i.e. the point were liquid, solid and air meet; in a 3D situation it would be a line) is moved determines the geometry of the boundary condition. Indeed two different orientation of the solid are encountered performing the variations.

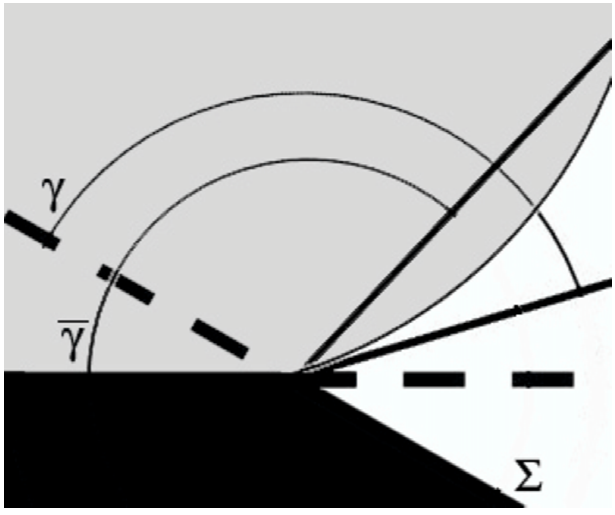

Figure 2.1: The contact angle of a drop (gray) in presence of a corner on the solid surface (black) must be in between the values relative to the two inclinations.

For a variation directed beyond the corner, considering the setting just described and the fact that the vector $\mathbf{N}$ points outside the drop, ϵ must be positive and the

condition for equilibrium is: $\mathcal{E}(\epsilon) - \mathcal{E}_0 \geq 0$ for any $\epsilon > 0$. It is possible to follow exactly the computation done in the previous section until the very last line, where with the chosen variation the condition becomes:

$$\oint_\Sigma \tau(\beta - \cos\gamma)\, ds \geq 0. \tag{2.18}$$

Similarly, with a variation in the opposite direction, equilibrium is reached if:

$$\oint_\Sigma \tau(\beta - \cos\tilde{\gamma})\, ds \leq 0. \tag{2.19}$$

Figure 2.1 may clarify the situation because the angles γ and $\bar{\gamma}$ are measured on different planes (lines in the 2D picture). The result is that there is a range of admissible values for the contact angle of the stationary state.

2.2 The phase field model

The shape equations just derived are the basis of any research on the physics of wetting phenomena. A rich although concise review can be found in [17]. However in many interesting situations an analytic solution is not available and also a numerical approximation is rather difficult. A first source of problems is the possible roughness of the solid surface: the possibility of inducing a high contact angle (bigger than 90°) on a water drop (hydrophobicity) is often a desired feature for a substrate. An appropriate roughness can improve it [2, 12, 34], but at the same time it may generate singularities. Another critical situation is the creation of new interfaces during a dynamical process: a drop can divide in two or more smaller drops under suitable conditions, or viceversa a merging is possible, this would contradict the hypothesis of an embedded surface.

Dealing with these issues within the geometric approach is often impossible. Phase field models are an attempt to overcome these difficulties.

2.2.1 Overview on the model

Phase field models and the equations governing them (for example Allen-Cahn and Cahn-Hilliard equations) move the attention from the interfaces to the phases -as the name itself suggests. The liquid drop will be considered as a subset of the physical domain and it will be denoted with ω. The geometry of the drop is described using a phase function ϕ that takes the value 1 in the liquid phase, the value 0 in the environmental fluid, and spans the whole $[0, 1]$ interval in a liquid-vapor transition

region. Thus the sharp interfaces of the (geometric) capillary model are replaced by narrow transition layers of width $\epsilon > 0$, a small parameter. The equilibrium shape of the drop is obtained by setting up a steepest descent dynamics for ϕ which tends to a state minimizing an ϵ-regularized version of the capillary energy. In the limit as ϵ tends to 0, we recover the solution of the capillary problem, with sharp interfaces between the phases. The presence of the solid is modeled by imposing suitable boundary conditions to the phase field function (both Neumann and Dirichlet conditions have been implemented). The model can be easily adapted to reproduce contact angle hysteresis, by changing the boundary conditions in order to account for the pinning effects on the contact line due to dissipation.

We introduce some different notations with respect to the previous section, in order to avoid confusions between the two approaches. As already said, the drop occupies the region ω, a subset of the computational/phisical domain Ω. Another subset of ω is considered as solid and denoted by S. The physical notation for the interfaces is recovered: $\partial_S\omega = \partial\omega \cap \partial S$ is the interface between liquid and solid, it will be called Σ_{SL}; $\partial_V\omega = \partial\omega \setminus \partial_S\omega$ is the liquid-vapor interface Σ_{LV}; $\partial S \setminus \partial\omega$ is the solid-vapor one, Σ_{SV}; ρ_L represents the density of the fluid (we will always consider a homogeneous fluid and we will set $\rho_L = 1$) and $U(x,t)$ is a generic potential related to an external force field (gravity, for example). We recall that the terms $\sigma_{AB}(x)$ are the surface energies (or surface tensions) at a point x on the AB interface. In the case of a homogeneous solid, these are constant and the capillary energy becomes:

$$\begin{aligned} E(\omega,t) &= \sigma_{SL}|\Sigma_{SL}| + \sigma_{LV}|\Sigma_{LV}| + \sigma_{SV}|\Sigma_{SV}| + \int_\omega U(x,t)\,d\mathcal{V}_x \\ &= (\sigma_{SL} - \sigma_{SV})|\Sigma_{SL}| + \sigma_{LV}|\Sigma_{LV}| + \int_\omega U(x,t)\,d\mathcal{V}_x + k \end{aligned} \tag{2.20}$$

where $|A|$ denotes the measure of the set A and k is a constant, that does not enter in the search for the minima of the functional and so it will be omitted. With the exception of the term due to the volume constraint, which will be soon be introduced, the energy in (2.20) is exactly the same as the one in (2.8).

The problem of capillarity can now be rephrased as:

$$\text{Given a volume } \mathcal{V} > 0, \text{ find } \omega^* = \operatorname*{argmin}_{|\omega|=\mathcal{V}} \{E(\omega,t)\}\,. \tag{2.21}$$

Laplace equation (2.9) is not affected by the change of notation (clearly the mean curvature now refers to Σ_{LV}), while it is useful to rewrite Young's law:

$$\cos\theta = -\frac{\sigma_{SL} - \sigma_{SV}}{\sigma_{LV}} =: \cos\theta^Y\,. \tag{2.22}$$

A phase field formulation for the problem is obtained by considering an energy of the type

$$E_\epsilon(\phi, t) = \int_\Omega \epsilon|\nabla\phi|^2 + \frac{1}{\epsilon}W(\phi) + \phi\, U(x,t)\, d\mathcal{V}_x \tag{2.23}$$

where ϕ is the phase function. The non-negative potential $W(\phi)$ vanishes only for the values of ϕ representing the vapor and the liquid phases. It is tuned in order to produce the correct interfacial surface tension values from the corresponding interphase transition layers in the limit as $\epsilon \to 0$.

2.2.2 Preliminars on $\Gamma-$convergence

$\Gamma-$convergence is widely accepted as the appropriate definition of variational convergence for a large class of problems. In other words, when one is interested in the convergence of the minimizers of a family of functionals, $\Gamma-$convergence often provides the right framework. Our phase field model shares this property, but we exploit the result in the opposite direction: usually the limit functional is a simplification of the "physical" $\epsilon-$dependent formulation, like for example the 2D theory of elastic shells obtained as the $\epsilon \to 0$ limit of the 3D elasticity of $\epsilon-$thick 3D shells. In the case of wetting, the "true" functional is the geometric one and instead we work with the $\epsilon-$approximation, with ϵ small but finite, which is more tractable numerically. The convergence of the minimizers as $\epsilon \to 0$ guarantees for the significance of the simulations.

An exhaustive presentation of the theory of $\Gamma-$convergence is out of the scope of this thesis, since my research was not involved with it. However, the understanding of what follows is contingent upon the knowledge of at least the basic properties of $\Gamma-$convergence, given below. We refer to the books of Dal Maso [20] and Braides [11] for a complete description of the theory and of its applications.

Let X be a metric space. This hypothesis may appear very limiting and indeed the results we will present are still true in a more general setting. However for the purpose of this overview, this situation allows for a more direct description and a better intuition of the mechanism behind the theory. A sequence of functionals $f_j : X \to \bar{\mathbb{R}}$ is said to $\Gamma-$converge in X to $f_\infty :\to \bar{\mathbb{R}}$ if for all $x \in X$:

- for every converging sequence $(x_j) \to x$ the *lim inf inequality* is satisfied

$$f_\infty(x) \leq \liminf_j f_j(x_j); \tag{2.24}$$

- there exists a *recovery* sequence $(\bar{x}_j)$ converging to $\bar{x}$ for which the *lim sup inequality* holds

$$f_\infty(\bar{x}) \geq \limsup_j f_j(\bar{x}_j); \tag{2.25}$$

Other equivalent definitions are possible. We preferred the one above because it is the most operative and it shows immediately the stability under continuous perturbation. If (f_j) $\Gamma-$converges to f_∞ and if $g : X \to \bar{\mathbb{R}}$ is continuous for the considered metric, then $(f_j + g)$ converges to $f_\infty + g$. Indeed:

$$f_\infty(x) + g(x) \leq \liminf_j f_j(x_j) + \lim_j g(x_j) = \liminf_j (f_j(x_j) + g(x_j)), \tag{2.26}$$

and if $(\bar{x}_j)$ is a recovery sequence for (f_j)

$$f_\infty(\bar{x}) + g(\bar{x}) = \lim_j f_j(\bar{x}_j) + \lim_j g(\bar{x}_j) = \lim_j (f_j(\bar{x}_j) + g(\bar{x}_j)). \tag{2.27}$$

Notice that, once the lim inf inequality is proved, the recovery sequence satisfies $f_\infty(\bar{x}) = \lim_j f_j(\bar{x}_j)$.

We want now to prove the announced property regarding the **convergence of the minima**. Following [11], we achieve this result in two steps.

Theorem 2.2.1. *If f_j $\Gamma-$converges to f_∞ in X and if $K \subset X$ is a compact set, then*

$$\inf_K f_\infty \leq \liminf_j \inf_K f_j. \tag{2.28}$$

While if $U \subset X$ is open

$$\inf_U f_\infty \geq \limsup_j \inf_U f_j. \tag{2.29}$$

Proof: Since K is compact it is possible to define a sequence $(\tilde{x}_j)$ such that $\liminf_j \inf_K f_j = \liminf_j f_j(\tilde{x}_j)$, and to extract a subsequence satisfying $\lim_k f_{j_k}(\tilde{x}_{j_k}) = \liminf_j \inf_K f_j$, while $\tilde{x}_{j_k} \to \bar{x} \in K$. If the sequence (x_j) is build as $x_j = \tilde{x}_{j_k}$ for $j = j_k$ and $x_j = \bar{x}$ otherwise, then:

$$\inf_K f_\infty \leq f_\infty(\bar{x}) \leq \liminf_j f_j(x_j) \leq \liminf_k f_{j_k}(x_{j_k}) = \lim_k f_{j_k}(\tilde{x}_{j_k}) = \liminf_j \inf_K f_j. \tag{2.30}$$

For any fixed value of $\delta > 0$, there exists $x \in U$ such that $f_\infty(x) \leq \inf_U f_\infty + \delta$. Hence, given a recovery sequence (x_j), one finds:

$$\inf_U f_\infty + \delta \geq f_\infty(x) \geq \limsup_j f_j(x_j) \geq \limsup_j \inf_U f_j. \tag{2.31}$$

Since δ is arbitrary, the theorem is proved. □

Theorem 2.2.2. *If the sequence* (f_j) *is* equi-mildly coercive *(i.e. if there exists a non-empty compact set* $K \subset X$ *such that* $\inf_X f_j = \inf_X f_j$ *for all* j*) and if* f_∞ *is the* $\Gamma-$*limit of* f_j*, then:*

$$\exists \min_X f_\infty = \liminf_j \inf_X f_j. \tag{2.32}$$

Proof: This theorem is an extension of the previous one. Let $\bar{x}$ be the same as in the proof above, then taking $U = X$ one obtains:

$$\begin{aligned} \inf_X f_\infty \leq \inf_K f_\infty \leq f_\infty(\bar{x}) \leq \liminf_j \inf_K f_j \\ = \liminf_j \inf_X f_j \leq \limsup_j \inf_X f_j \leq \inf_X f_\infty \end{aligned} \tag{2.33}$$

□

Under some more assumption it is possible to prove the convergence of the minimizers. Notwithstanding the key role of this property for our analysis, a precise statement of this theorem is out of the purposes of this introduction. A deep discussion about it can be found in [20]. The hypothesis under which our results share this property will be highlighted in the following sections concerning the asymptotic behavior of the phase field functional (2.23).

2.2.3 Dirichlet boundary conditions

In [53] we considered two alternative formulations, one based on Dirichlet boundary conditions, one based on Neumann boundary conditions. In our model the solid surface supporting the drop is introduced through a suitable boundary condition. We present in this section and in the following one the statements and the proofs that support our phase field formulation.

The analysis performed rests on a slight modification of results by Baldo and Bellettini [7] and Modica [38]. However there exists a wide mathematical literature on this topic starting from ideas of Modica and Mortola [39]. The main new feature is the introduction of a boundary condition at the solid through a phase value that is not a zero of the potential.

The construction starts with the definition of:

$$\bar{E}_\epsilon(\phi) = \begin{cases} E_\epsilon(\phi) & \text{if } \phi \in H^1(\Omega, \mathbb{R}^2) \text{ and } \phi|_{\partial\Omega} = g, \\ +\infty & \text{otherwise in } L^1; \end{cases} \tag{2.34}$$

$$\bar{E}_0(\phi) = \begin{cases} E(\{\phi \equiv L\}) & \text{if } \phi \in BV(\Omega, \{V, L\}), \\ +\infty & \text{otherwise in } L^1; \end{cases} \tag{2.35}$$

where g is the function that gives the physically relevant Dirichlet boundary condition, to be specified later,and V, $L \in \mathbb{R}^2$ are the values corresponding to the vapor and the liquid phase. It is possible to prove that if ϕ_ϵ^* is a family of minimizers of $\bar{E}_\epsilon$ and if ϕ^* is its limit in L^1 (the existence of the limit is part of the proof), then the first component of ϕ^* is the characteristic function of a solution for the capillary problem (2.21), while the second one is 0 everywhere.

The external force term does not depend on ϵ (see equation (2.23)) and it can be treated separately. Indeed, as shown in section §2.2.2, the continuity in the desired topology is enough for this procedure. In this case $\phi \mapsto \int \phi U \, d\mathcal{V}_x$ is continuous for the L^1 topology if U is regular enough. The gravitational potential, for example, is admissible.

The problem is set in Ω, a bounded subset of $\mathbb{R}^n$ (for $n = 2, 3$) with piecewise $\mathcal{C}^2$ and Lipschitz boundary. It is decomposed in two parts: $\partial\Omega = \partial_S\Omega \cup \partial_V\Omega$ (the set $\partial_S\Omega$ coincides exactly with what we called ∂S in (2.20)). For $\psi = (\psi_1, \psi_2) \in \mathbb{R}^2$, the potential is $W(\psi) = a^2\psi_1^2(1-\psi_1)^2 + b^2\psi_2^2$, where:

$$a = 3\sigma_{LV} > 0, \tag{2.36}$$

$$b = \frac{1}{2}(\sigma_{SV} + \sigma_{SL} - \sigma_{LV}) > 0 \tag{2.37}$$

Denote by $L = (1, 0)$ and $V = (0, 0)$ the only two zeros of W, as announced. In fact, we want the phase function to assume only two values, since the solid phase is modeled through a boundary condition. Let $g : \partial\Omega \to \mathbb{R}^2$ such that $g \equiv V$ on $\partial_V\Omega$ and $g \equiv (\phi_S, 1) := S$ on $\partial_S\Omega$, where ϕ_S is the unique solution of

$$\cos\theta^Y = -4\phi_S^3 + 6\phi_S^2 - 1 \qquad 0 \le \phi_S \le 1. \tag{2.38}$$

Theorem 2.2.3. *The functional $\bar{E}_0$ given by (2.34) is the $\Gamma-$limit of $\bar{E}_\epsilon$, given by (2.35), as ϵ tends to zero in the topology of L^1.*

Moreover if for every $\epsilon > 0$ we define $\phi_\epsilon^* = argmin\{\bar{E}_\epsilon(\phi) : \int_\Omega \phi_1 = \mathcal{V}\}$, then the sequence (ϕ_ϵ^*) is pre-compact in L^1. Every cluster point, say ϕ^*, belongs to $BV(\Omega, \{V, L\})$ and we have $\phi = argmin\{\bar{E}_0(\phi) : \int_\Omega \phi_1 = \mathcal{V}\}$.

Proof:

The proof uses classical arguments, but we give here some details because they are essential in the construction of the numerical scheme presented hereafter. The discussion entails two steps: in the first a link between our problem and that considered by Baldo and Bellettini [7] is established. After that the volume constraint is considered and inserted in the convergence result.

In the cited paper the $\Gamma-$limit of functional $\bar{E}_\epsilon$ is recognized as:

$$\begin{aligned}\tilde{E}_0(\phi) =& 2d\,(V,L)\,\mathcal{H}_{n-1}(\partial^*\{\phi\equiv L\}\cap\partial^*\{\phi\equiv V\})+\\ &+2\int_{\partial\Omega} d(\phi|_{\partial\Omega}(x),g(x))d\mathcal{H}_{n-1}(x),\end{aligned} \tag{2.39}$$

defined on $BV(\Omega,\{V,L\})$. The symbol ∂^*A denotes the reduced boundary of the set A and $\mathcal{H}_{n-1}$ denotes the Hausdorff measure of dimension $n-1$. The distance d can be defined in some different but equivalent ways. The most treatable one is:

$$d(v_1,v_2)=\min\left\{\int_{-\infty}^{+\infty}\left\{\dot{\rho}^2+W(\rho)\right\}dt\quad \rho(-\infty)=v_1,\rho(+\infty)=v_2\right\}. \tag{2.40}$$

The point is now to show that in our situation $2\bar{E}_0=\tilde{E}_0$. In the wetting setting, we label as "liquid" the set $\{\phi\equiv L\}$ and the set $\{\phi\equiv V\}$ "vapor". Moreover, considering our choice of g, the functional (2.39) becomes:

$$\tilde{E}_0(\phi)=2d(V,L)|\Sigma_{LV}(\phi)|+2d(V,S)|\Sigma_{SV}(\phi)|+2d(S,L)|\Sigma_{SL}(\phi)|. \tag{2.41}$$

Indeed the integral in (2.39) decomposes into the sum of two terms because g is constant and ϕ can assume only the values V and L [7]. Then we have only to show that equation (2.38) and the metric (2.40) give us the correct value for the surface tensions if we chose appropriately the values of the parameters a and b in the potential. The condition for them are:

$$\begin{aligned}\sigma_{LV}=d(L,V)&=\min\int_{-\infty}^{+\infty}\{\dot{\rho}_1^2+W((\rho_1,0))\}dt\\ &=2\int_0^1\sqrt{W((\tau,0))}d\tau=\frac{a}{3}\end{aligned} \tag{2.42}$$

$$\begin{aligned}\sigma_{SV}=d(S,V)&=2\int_0^{\phi_S}\sqrt{W((\tau,0))}d\tau+2\int_0^1\sqrt{W((0,\tau))}d\tau\\ &=-2a\left(-\frac{\phi_S^2}{2}+\frac{\phi_S^3}{3}\right)+b\end{aligned} \tag{2.43}$$

$$\begin{aligned}\sigma_{SL}=d(S,L)&=2\int_{\phi_S}^1\sqrt{W((\tau,0))}d\tau+2\int_0^1\sqrt{W((0,\tau))}d\tau\\ &=2a\left(\frac{1}{6}-\frac{\phi_S^2}{2}+\frac{\phi_S^3}{3}\right)+b,\end{aligned} \tag{2.44}$$

and hence the requirements are $b=\frac{1}{2}(\sigma_{SL}+\sigma_{SV}-\sigma_{LV})$ and exactly equation (2.38). Notice that the condition $b>0$ can always be reached because we can add the same quantity to σ_{SV} and σ_{SL} without changing the problem: the only physically relevant quantity is the difference $\sigma_{SV}-\sigma_{SL}$. Finally, we observe that the form of W implies

that the minimal ϕ_2 is always the constant 0, also if this value does not match the boundary condition. Thus from now on, we will write simply ϕ instead of ϕ_1.

Having established the link with the setting of [7], the proof of the Γ-convergence result can be easily adapted to this case. Handling the volume constraint is not a difficult task [1, 11, 20]. The subspace $\{\phi \in L^1, \int \phi_1 = \mathcal{V}\}$ is closed in the L^1 topology and, in the recovering sequence of the $\Gamma - \limsup$, we can always assume $\int \phi_\epsilon = \int \phi$. □

The external force field can be easily added at this point. From the theorem we know that when ϵ goes to zero the minimizers of $\bar{E}_0$ are functions in $BV(\Omega, \{V, L\})$. More precisely the first component will take the value 1 in the region occupied by the liquid and the value 0 in the vapor region. Hence, looking at (2.20) and (2.23), we obtain

$$\int_\Omega \phi_1 \, U(x,t) \, d\mathcal{V}_x = \int_\omega U(x,t) \, d\mathcal{V}_x \tag{2.45}$$

as desired.

2.2.4 Neumann boundary conditions

An alternative approach to the phase field formulation can be based on Neumann-type boundary conditions. For this purpose, we use a result of Modica [38]. We consider, for simplicity, the situation of a region $\Omega \subseteq \mathbb{R}^3$ whose boundary is the solid surface S. Inside this set we want to solve the capillary problem for a prescribed volume of liquid L. In the sequel we will not discuss explicitly the volume constraint, which can be added later exactly as before. The formulation is based on a potential of the type $W(x) = a^2x^2(1-x)^2$ (with $a > 0$ to be specified later), while in [38] the minima of the potential should be strictly positive: this limitation can be removed by choosing appropriately the boundary term (see the functional (2.48) below).

Let $\sigma : [0; +\infty) \to \mathbb{R}^+$ be any continuous function and define

$$\hat{\sigma}(x) = \inf_{s \geq 0} \left\{ \sigma(s) + 2 \left| \int_x^s \sqrt{W(y)} \, dy \right| \right\}, \tag{2.46}$$

$$c_0 = \int_0^1 \sqrt{W(y)} \, dy. \tag{2.47}$$

Consider the functional

$$E_\epsilon^N(\phi) = \begin{cases} \int_\Omega \epsilon |D\phi_\epsilon|^2 + \frac{1}{\epsilon} W(\phi_\epsilon) \, dx + \int_{\partial\Omega} \sigma(\tilde{\phi}_\epsilon) \, d\mathcal{H}_{n-1}(x) & \text{if } \phi \in H^1(\Omega, \mathbb{R}), \\ +\infty & \text{otherwise in } L^1. \end{cases} \tag{2.48}$$

where $\tilde{\phi}_\epsilon$ denotes the trace of ϕ_ϵ on the boundary. Then E_ϵ^N Γ-converges to [38]

$$E_0^N(\phi) = 2c_0 \left|\Sigma_{LV}\right| + \hat{\sigma}(1) \left|\Sigma_{SL}\right| + \hat{\sigma}(0) \left|\Sigma_{SV}\right|. \tag{2.49}$$

The physical interpretation of the convergence result is the following. Choose, as in [48], $\sigma(x) := Nx$, where N is a constant to be tuned in order to model the right contact angle. The Euler-Lagrange equations for (2.48) yields the Neumann-type boundary condition

$$-2\epsilon \frac{\partial \phi}{\partial n} = N. \tag{2.50}$$

Here n is the outward unit normal vector to $\partial\Omega$. By an appropriate choice of a and N the correct surface tensions can be recovered. This is an easy calculation:

$$2c_0 = \frac{a}{3} = \sigma_{LV}, \tag{2.51}$$

$$\hat{\sigma}(0) = 0, \tag{2.52}$$

$$\hat{\sigma}(1) = \inf_{s \geq 0} \left\{ Ns + 2a \left(\frac{s^3}{3} - \frac{s^2}{2} + \frac{1}{6} \right) \right\} = \sigma_{SL} - \sigma_{SV}. \tag{2.53}$$

The hypothesis on the sign of the function $\sigma(\cdot)$ restricts our study to values $N \geq 0$ and thus to contact angles $\theta^Y \geq \frac{\pi}{2}$. The model for acute contact angles can be obtained by putting $\phi \equiv 0$ in the liquid phase and $\phi \equiv 1$ in the vapor. It is easy to see that in the Euler-Lagrange equation this exchange produces the same results than considering negative values of N in the usual representation. In any case, the study of the minimum problem (2.53) gives a non-linear equation that chooses the right value of N for the desired contact angle.

2.3 Contact angle hysteresis: incremental formulation for quasistatic evolution

We conclude the mathematical and physical presentation of the problem with the description of the model followed when considering time evolution problems. In the static case considered so far, in every simple geometry, the contact angle has unique value, the Young contact angle given by (2.22) and which depends only on the chemistry of the three phases S, L, V. In reality, something different happens if the system is perturbed. If the solid surface is inclined, the drop partially evaporate, or it is inflated, the contact angle changes and hence the overall shape of the liquid-vapor interface changes as well.

Following [3, 25], we consider the following discrete incremental formulation for the problem of the quasistatic evolution of a drop. Given the configuration $\omega^*(t)$ of a drop at time t, the one at time $t+\delta t$ is given by:

$$\omega^*(t+\delta t) = \operatorname*{argmin}_{|\omega|=\mathcal{V}(t+\delta t)} \{E(\omega, t+\delta t) + D(\omega, \omega^*(t))\} \tag{2.54}$$

where the dissipation $D(\omega_1, \omega_2)$ is given by

$$D(\omega_1, \omega_2) = \mu |\partial_S \omega_1 \triangle \partial_S \omega_2|. \tag{2.55}$$

Here $A \triangle B = (A \setminus B) \cup (B \setminus A)$ denotes the symmetric difference of the sets A and B and $\mu > 0$ is a parameter giving the dissipated energy per unit variation of the wetted area. A simple example to illustrate the meaning of this formulation can be the case of a drop on a horizontal plane, subject to no gravity. It can be shown that, in this case, $\omega^*(t)$ is always a spherical cap [29]. Thus energy and dissipation can be written as:

$$E = (\sigma_{SL} - \sigma_{SV})\pi a^2 + \sigma_{LV} A \tag{2.56}$$

$$D(\omega_1, \omega_2) = D(a_1, a_2) = \mu\pi |a_1^2 - a_2^2|. \tag{2.57}$$

where $A = 2\pi Rh$ is the area of the spherical cap of radius R and height h, while a is the radius of the wetted area, that is the interface between the solid and the liquid. In this situation the variations of A at fixed volume $|\omega| = \mathcal{V}(t+\delta t)$ become:

$$\delta A|_{|\omega|=\mathcal{V}(t+\delta t)} = 2\pi a \cos\theta \, \delta a. \tag{2.58}$$

Therefore, the Euler-Lagrange equation for the incremental variational problem are:

$$-(\sigma_{SL} - \sigma_{SV})2\pi a - \sigma_{LV} \cos\theta \, 2\pi a \in \partial \mu\pi |a^2 - a^2(t)|, \tag{2.59}$$

where

$$\partial \mu\pi |a^2 - a^2(t)| = \begin{cases} \{2\pi a\mu\} & \text{if } a > a(t) \\ \pi a[-\mu, \mu] & \text{if } a = a(t) \\ \{-2\pi a\mu\} & \text{if } a < a(t) \end{cases} \tag{2.60}$$

is the sub-differential of the convex function $a \mapsto \mu\pi |a^2 - a^2(t)|$. Another way to see that is to consider left and right variation for the parameter a, exactly as in the case of a non-smooth solid. In any case, the result is the following:

$$\cos\theta \in \begin{cases} \{\cos\theta^r\} & \text{if } a < a(t) \\ [\cos\theta^r, \cos\theta^a] & \text{if } a = a(t) \\ \{\cos\theta^a\} & \text{if } a > a(t) \end{cases} \tag{2.61}$$

where

$$\cos\theta^a = \cos\theta^Y - \frac{\mu}{\sigma_{LV}} \tag{2.62}$$

defines the *advancing contact angle* and

$$\cos\theta^r = \cos\theta^Y + \frac{\mu}{\sigma_{LV}} \tag{2.63}$$

defines the *receding contact angle*.

Thus, the incremental problem is: minimize

$$F(\omega, t+\delta t) = (\sigma_{SL} - \sigma_{SV})|\partial_S\omega| + \sigma_{LV}|\partial_V\omega| + \mu|\partial_S\omega \triangle \partial_S\omega(t)| \tag{2.64}$$

by the phase field method discussed previously. In the Dirichlet case, the numerical scheme will try to solve:

$$\phi_\epsilon^*(t+\delta t) = \text{argmin}\left\{E_\epsilon(\phi, t+\delta t), \text{subject to } \int_\Omega \phi = \mathcal{V}(t+\delta t)\right\} \tag{2.65}$$

with

$$\phi = \begin{cases} \phi_S^a & \text{on } \partial\Omega_\epsilon^a \\ \phi_S^r & \text{on } \partial\Omega_\epsilon^r \end{cases} \tag{2.66}$$

where ϕ_S^a and ϕ_S^r are the Dirichlet boundary conditions associated with the advancing and the receding angle respectively, computed with an equation similar to that in (2.38) and

$$\partial\Omega_\epsilon^r \simeq \partial\Omega \cup \partial_S\omega \quad \text{(receding contact zone)}, \tag{2.67}$$

$$\partial\Omega_\epsilon^a \simeq \partial\Omega \setminus \partial_S\omega \quad \text{(advancing contact zone)}. \tag{2.68}$$

The appropriate Neumann boundary conditions are imposed in exactly the same manner. The two situations differ only in the resulting shape of the contour lines of ϕ in a small neighborhood of the contact line. A detailed comparison is given in section §3.4.1.

Chapter 3

WETTING: basic numerical techniques and 2D simulations

3.1 Introduction to algorithms and approximations

The phase field formulation of wetting problem is more suitable for numerical simulation than the geometric one because of the relative simplicity of the equations governing it and the possibility to treat complicated solid geometries. However an appropriate algorithm is needed to make functional (2.34) stationary and many choices has to be made for the discretization of the problem.

The first issue is how to implement the volume constraint. We opt for a Lagrange multiplier because of its physical meaning (recall Laplace law (2.9)). Consequently, the Euler-Lagrange equation for the phase field model becomes (here $U = 0$ and $a = 1$ for simplicity):

$$\begin{cases} -\epsilon \triangle \phi + \dfrac{1}{\epsilon}\phi(1-\phi)(1-2\phi) + \lambda = 0 & \text{in } \Omega \\ \phi = \phi_S & \text{on } \partial_S\Omega \\ \phi = 0 & \text{on } \partial_V\Omega \end{cases} \tag{3.1}$$

where the value of λ has to be calculated in order to match the constraint $\int \phi = \mathcal{V}(t)$.

To solve the equilibrium equation, the problem is transformed into a parabolic PDE generated by a gradient flow [8]. Hence the system will follow an artificial relaxation dynamics until, at convergence, it reaches the configuration solving equation (3.1). The gradient flow is introduced by setting $\phi = \phi(\tau, x)$, where τ is a

fictitious time, and solving:

$$\phi_\tau = \epsilon \triangle \phi - \frac{1}{\epsilon}\phi(1-\phi)(1-2\phi) - \lambda. \tag{3.2}$$

Here the Laplacian is calculated with respect to the space derivatives, while the subscript τ denotes a time derivative. The solution of the original equation (3.1) is obtained in the limit $\lim_{\tau\to+\infty}\phi(\tau,\cdot)$. In fact, along long the flow (3.2), the energy is decreasing in time

$$\frac{d}{d\tau}E_\epsilon = -2\int_\Omega |\phi_\tau|^2\, dx \leq 0. \tag{3.3}$$

The discretization technique chosen for the first simple calculations is the one given by finite differences. However, in the next section we will show that they can be properly adapted to solve real 3D situations.

Different schemes for the time integration are possible: explicit, implicit and mixed ones. As we will illustrate in section §3.2, there are no significant advantages using complicated schemes. Therefore we present here the simplest explicit scheme (forward Euler), considering also that only slight modifications are needed to recast what follows in the other cases.

A splitting method is employed in order to find at each iteration the correct value for the Lagrange multiplier associated with the volume constraint λ. Namely, given an initial guess ϕ^0 that satisfies the good boundary condition the scheme for the Dirichlet case reads (the conversion for Neumann case is straightforward):

$$\phi^{N+\frac{1}{2}} = d\tau\left(\epsilon \triangle \phi^N - \frac{1}{\epsilon}\phi^N(1-\phi^N)(1-2\phi^N)\right) + \phi^N \tag{3.4}$$

$$\lambda^N = \frac{\mathcal{V} - \int_\Omega \phi^{N+\frac{1}{2}}}{\int_\Omega 1} \tag{3.5}$$

$$\phi^{N+1} = \phi^{N+\frac{1}{2}} + \lambda^N \tag{3.6}$$

where $\mathcal{V} = \int_\Omega \phi^0$. By construction, $\int_\Omega \phi^N = \mathcal{V}$ stays constant during the iterations.

For the space derivatives we use instead a high order approximation nine-point stencil that is classical in the 2-D case, but non trivial in the axisymmetric one. The derivation can be found in [13].

3.2 Explicit, implicit or mixed algorithms

The algorithm just described (3.4-3.6) is an explicit Euler scheme. From the computational point of view (we left any consideration regarding the stability to the next

section) it requires only simple manipulation to the matrix containing the value of ϕ on the nodes.

If a faster convergence is needed (although the performance of the explicit scheme are already satisfactory), many other possibilities are present in literature. We tested two of them: a semi-implicit backward Euler scheme and a unbalanced first order approximation scheme described by Shen and others in [55].

The backward Euler scheme is obtained from the explicit one simply by taking $\triangle\phi^{N+1}$ instead of $\triangle\phi^N$ in (3.4). This change implies the resolution of a linear system at each iteration of the algorithm, but since the matrix does not change (if the physical conditions of the systems remain fixed) a single LU factorization can return a solution at the cost of a matrix product. However summing up the costs of the initial factorization and of the subsequent matrix products, the advantage of this choice (a lower number of iterations to reach convergence) is lost, as the table below shows.

Shen algorithm shares many features with the backward Euler scheme, but it prevents oscillations and in some cases it speeds up convergence. Also for this scheme a splitting algorithm is needed to find the correct value of λ, while ϕ is calculated following the rule:

$$\begin{aligned}\frac{3\phi^{N+1}-4\phi^N+\phi^{N-1}}{2d\tau} = &\epsilon\triangle\phi^{N+1}-\frac{1}{\epsilon}\left(\phi^N(1-\phi^N)(1-2\phi^N)\right)+\\ &+\frac{s}{\epsilon}\left(\phi^{N+1}-2\phi^N+\phi^{N-1}\right)+\lambda^N.\end{aligned} \tag{3.7}$$

Here s is a parameter that can be chosen in the interval $[1,5]$. In our tests the best results are obtained with $s=5$, as in Shen paper.

The timings obtained with these three algorithm are showed in the table below. For the test we employed a 100×100 grid and we calculated the computer time and the iterations needed to transform a rectangle to the correct disk corresponding to a 2D drop with a contact angle of 120 degrees. The number of iterations is related to the value of $d\tau$ which cannot be too large, otherwise the algorithm would not be stable. With a smaller grid, the implicit scheme is much more convenient, while with a larger one the results are comparable.

scheme	τ	iter to converge	cpu time (seconds)
explicit	0.001	1650	1308,7
	0.0011	1700	1344,3
	0.0012	1450	1145,7
	0.0013	1350	1068,3
implicit	0.005	1300	1506.4
	0.006	1100	1276.5
	0.007	1000	1158,1
shen	0.006	1300	1505
	0.006	1150	1331,2
	0.007	1000	1158,8

3.3 Stability considerations

The gradient flow technique shows a very stable behavior, once the parameter of the simulations are well tuned. A few numerical experiments are enough to observe the main features of this kind of algorithms: if ϵ is set too small (with respect to the grid spacing h) the level curves of ϕ lose smoothness and mobility. If the volume of the drop is too small with respect to the transition width (and hence with respect to ϵ), the algorithm is not stable. And the most important limit is represented by the fact that if a too large τ is chosen, the scheme diverge. A stability analysis of the algorithm can explain these facts and it helped the development of the 3D code. Therefore we include here also the results for a three dimensional simulation.

In this situation one needs to go beyond the classical Neumann stability analysis, which can be performed only for linear equations. The best results follows from a method explained in [35]. We will focus on the explicit scheme with a 5 points Laplacian for the 2D case and a 7 points Laplacian for the 3D. We will omit the λ term, because it is known that low order terms do not affect the stability of the scheme (see, [49] for example). The algorithm can be rewritten in a compact form:

$$\frac{\phi_{i,j}^{n+1} - \phi_{i,j}^{n}}{\tau} = 2\epsilon \left(\frac{-4\phi_{i,j}^{n} + \phi_{i+1,j}^{n} + \phi_{i-1,j}^{n} + \phi_{i,j+1}^{n} + \phi_{i,j-1}^{n}}{h^2} \right) - \frac{1}{\epsilon} f(\phi_{i,j}^{n}), \quad (3.8)$$

where f is the derivative of our potential $W(x) = Kx^2(1-x)^2$, K is the factor that have to match the physical parameter σ_{LV} in the Γ-convergence (we can suppose for the moment that $K = 1$). Round-off and approximations will create some error on the solution ϕ, the idea is to introduce them and to control their growth in order

to get stability. More precisely we replace $\phi_{i,j} \sim \phi_{i,j} + r_{i,j}$. Subtracting the exact equation from the approximated one the result is:

$$\frac{r_{i,j}^{n+1} - r_{i,j}^{n}}{\tau} = \frac{2\epsilon}{h^2}\left(r_{i+1,j}^{n} + r_{i-1,j}^{n} + r_{i,j+1}^{n} + r_{i,j-1}^{n}\right) + \left(-\frac{8\epsilon}{h^2} - \frac{1}{\epsilon}f'(\phi_{i,j}^{n})\right) r_{i,j}^{t} \quad (3.9)$$

In the last term we make another substitution that is the key point of this method: we take a Taylor expansion of $f(\phi + r) \simeq f(\phi) + f'(\phi)r$, since the error has to be small with respect to the solution. Keeping only r^{n+1} on the left we obtain:

$$r_{i,j}^{n+1} = \frac{2\tau\epsilon}{h^2}\left(r_{i+1,j}^{n} + r_{i-1,j}^{n} + r_{i,j+1}^{n} + r_{i,j-1}^{n}\right) + \left(1 - \frac{8\epsilon d\tau}{h^2} - \frac{d\tau}{\epsilon}f'(\phi_{i,j}^{n})\right) r_{i,j}^{t} \quad (3.10)$$

At this point the analysis splits into two parts: the liquid and the vapour zone will be considered first, and then the interface. If $\phi \simeq 0$ (vapour) or $\phi \simeq 1$ (liquid), than $f'(\phi) = 2K(1 - 6\phi + 6\phi^2) > 0$ and $f'(\phi) \simeq 2K$. So the equation for r^{n+1} can be seen as a weighted sum: since the sum of the coefficients is $1 - \frac{\tau}{\epsilon}f'(\phi_{i,j}^{n}) < 1$, if they are all positive, the following inequality holds:

$$r_{i,j}^{t+1} \leq \left(1 - \frac{\tau}{\epsilon}f'(\phi_{i,j}^{n})\right) \max_{i,j}\{r_{i,j}^{n}\}, \quad (3.11)$$

that means stability. Therefore the algorithm is stable if all the coefficients of the sum are positive, which implies:

$$\tau < \frac{\epsilon h^2}{8\epsilon^2 + 2Kh^2} \quad (3.12)$$

The interface does not enter in the stability condition, unless it is too wide with respect to the computational box. The worst possible case for the previous estimate is a situation in which $\phi = 0.5$ in the whole interface and hence $f'(\phi) = -K$. Supposing $r_{i,j}^{n} = r^n$ for all i, j and denoting with N the number of computational nodes and M the number of nodes in the interface, we have:

$$\sum r^{n+1} = \left(N\left(1 - \frac{2K\tau}{\epsilon}\right) + 3K\frac{\tau}{\epsilon}M\right) r^n. \quad (3.13)$$

The stability is maintained if $\sum r^{n+1} < \sum r^n = Nr^n$ and this is true if $M < \frac{2}{3}N$. Clearly in a normal simulation this condition is always satisfied ($N = 10000$, $M \simeq 4\sqrt{N} = 400$).

The 3D case is very similar. The only modification is that now the coefficient of the central point in the stencil is 6 instead of 4 (and obviously there are the contribution of the points in the third direction). It is easy to see that now the sufficient condition for stability is:

$$\tau < \frac{\epsilon h^2}{12\epsilon^2 + 2Kh^2} \quad (3.14)$$

The accordance of this analysis with the simulation is very accurate. If, as we usually do in the 2D case, we take $\epsilon = 0.008$, $h = 0.01$, $K = 1$, the bound predicted on the time increment is $\tau < 0.0011$. In the computations we found that the scheme converges also for $\tau = 0.0013$ but this value is very close to the predicted one. Similar results are obtained in the 3D case.

3.4 2D simulations

The simulation of this section shows how rich a behavior can be captured in spite of the simplicity of the approach. The efforts towards devising more efficient schemes in order to make large scale simulations possible will be described in the following chapter.

The computational grid is of 100×100 points regardless of the physical size of the objects simulated. With such a grid, we can set $\epsilon = 0.008 \cdot a$ where a is the coefficient in the potential (2.36). This assures interfaces of width $\simeq 5$ grid points: a value small enough with respect to the size of the drop, but sufficient for a good resolution of the shape of the interface.

The value of $d\tau$ depends on the evolution scheme. For the forward Euler scheme we set $d\tau = 0.001$, while we can reach $d\tau = 0.005$ for the semi-implicit scheme.

In the 2-D simulations we use a trapezoidal rule for the quadrature, while we pass to the Cavalieri-Simpson rule in the axisymmetric cases. We follow [49] for the condition on the symmetry axis in order to ensure a second order accuracy. The convergence of the schemes is tested on the time gradient. We always obtain a value for this estimator below 10^{-9} summing the contribution of all the computational nodes.

A remark about the size of the simulated drops is in order. If gravity is set to zero, the capillary problem is purely geometric and the length scale is irrelevant. In a realistic situation gravity can never be zero, but there is a typical length on which it acts: it is the *capillary length*, $\kappa^{-1} := \sqrt{\sigma_{LV}/\rho g}$ (usually for water in contact with air is of the order of some mm [17]). If the size of the drop is much smaller than this value, then capillary forces dominate gravity. Thus, setting $G = 0$ means to consider very small drops. In each case, when gravity is non zero, the length scales for which the simulation is relevant will be specified.

3.4.1 Contact angle hysteresis

We consider a drop on a plane and we increased and then decreased its volume in order to observe the hysteresis of the contact angle. This simulation is performed in order to obtain a benchmark case. Indeed the analytic solution for this problem is known: it is a spherical cap that does not move its base until the advancing (or the receding) contact angle is reached. Knowing this, we test our approach with an axisymmetric formulation.

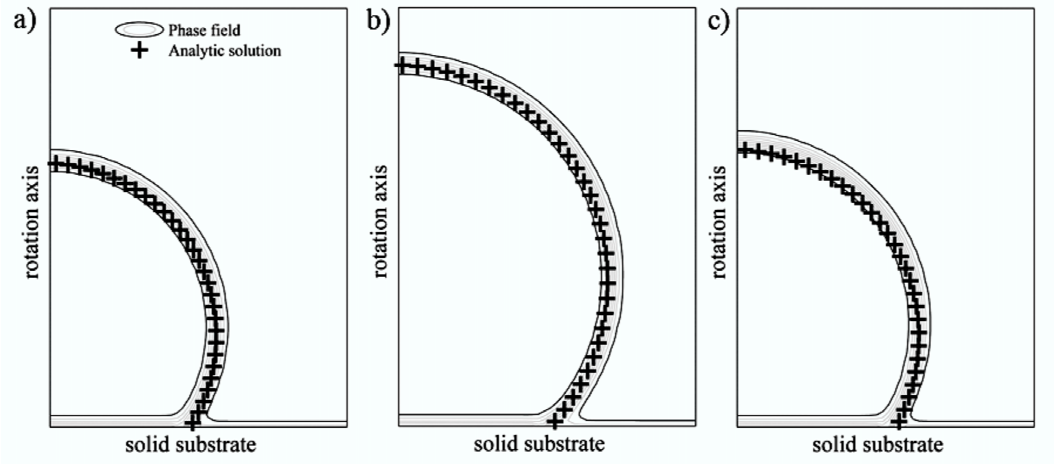

Figure 3.1: Inflating the drop causes first an increase of the contact angle with no motion of the contact line (a). With a further volume increment the drop advances (b). If the volume is then decreased, the first effect is only a modification of the contact angle, with fixed contact area (c).

Each time volume is added (or subtracted), we solve the gradient flow and we compare the phase field solution with the analytic sharp interface one (see Figure 3.1-3.2). The agreement is satisfactory: the analytic solution is always inside the contour lines of the transition layer from 1 (liquid) to 0 (vapor). A comparison between the two formulation proposed shows that the Neumann scheme outperforms the Dirichlet one in simulating the hysteresis phenomenon. More precisely the differences are visible in the receding stage in a hydrophobic situation, or during the advancing stage in a hydrophillic case (see Figures 3.1, 3.2 and the discussion below).

The main difficulty here is the treatment of the triple junction among the three phases (solid, liquid and vapor) in the diffuse interface setting. We overcome this problem by defining a third zone on the solid boundary, which can be subdivided into two parts: the semi-wet and the semi-dry zones.

We proceed as follows. On the row of computational nodes above the solid, the transition point between values smaller or larger than 0.5 is recognized and it

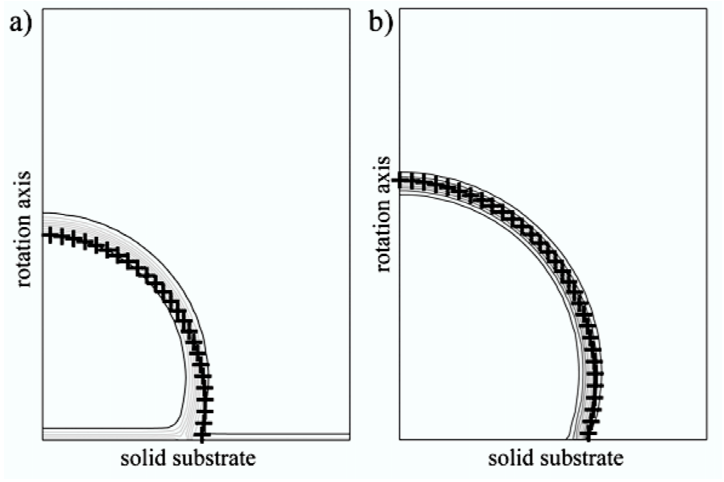

Figure 3.2: A receding drop simulated with a Dirichlet BC (a) and with a Neumann BC (b).

is projected this on the solid. The semi-wet zone (respectively semi-dry) consists of the 2 nodes from this point towards the liquid (toward the vapor). The desired stabilization is reached decreasing (increasing) by 15 degrees the angle that the Neumann boundary condition would impose in those points. For the Dirichlet scheme a modification of 20 degrees is needed. The situation is summarized with a graph in Figure 3.3, where the contour lines of a drop with a Young contact angle of 120 degrees are drawn. The algorithm proceeds as described in Section §2.4: starting from the solution at time t, we identify the three zones on the solid surface; we then calculate the solution at time $t + \delta t$ (i.e. with an increased or decreased volume) keeping fixed the boundary conditions calculated from the previous step. For this procedure the Neumann scheme is more precise, because the contour lines are not bent by the solid surface. This explains the improvement passing from panel a) to panel b) in Figure 3.2.

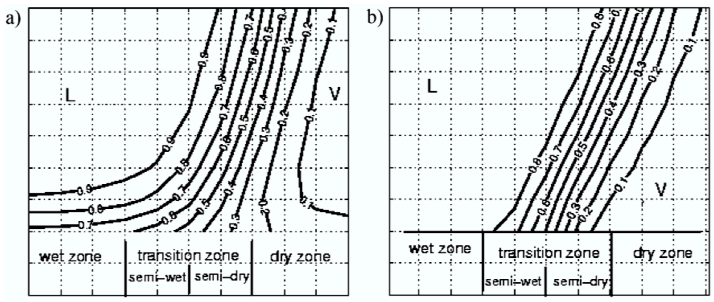

Figure 3.3: The determination of the different zones on a solid surface modeled by Dirichlet BC (a) and Neumann BC (b).

Because of these results, the Neumann scheme will be preferred dealing with hysteresis. The Dirichlet formulation will be used when considering non-smooth geometries for the solid (i.e. when the normal derivative cannot be directly defined) and dissipation effects are not the main interest.

3.4.2 Moving plates

Inspired by the striking experiments of A. Lafuma and D. Quéré [34], we consider the case of a drop compressed between two plates.

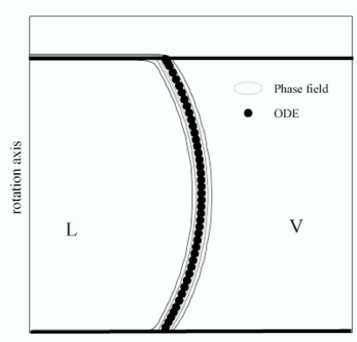

Figure 3.4: We check the initial position of the phase field solution with the shape given by the integration of the geometric ODE.

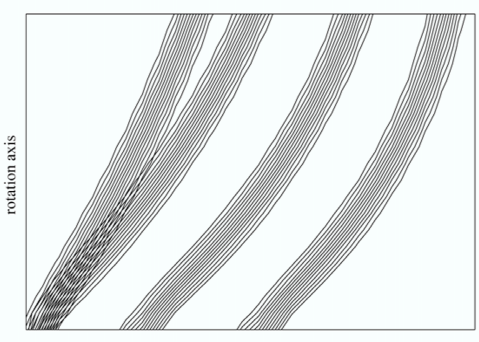

Figure 3.5: Evolution of the front near the lower plate during the compression, see the initial modification of the contact angle.

Our results are plotted in Figure 3.4-3.5. What we could observe with these simulation are the macroscopic effects of hysteresis. Energy minimizers are again axisymmetric. Figure 3.4 compares the phase field solution with the solution of the ODE arising from the sharp interface formulation.

The procedure to simulate the quasi-static movements of the plates is based on a sort of "predictor-corrector" scheme. Starting from a stable state, we cancel (add, respectively) a computational row at half the distance from the plates in order to obtain a compression (decompression). The prediction stage is done by looking for an energy minimization while keeping fixed artificially the wetted zones over the plates. In the correction stage we release this constraint: if the equilibrium configuration of the prediction stage has reached or even overcome the advancing (receding) contact angle, then a new minimization is performed. Otherwise the previous shape is accepted (see Figure 3.6). In this way we do not loose information about the history of positions of the liquid-solid interface, that are essential to resolve the hysteresis of the contact angle.

Figure 3.5 collects a sequence of snapshot of the evolution of the profile near

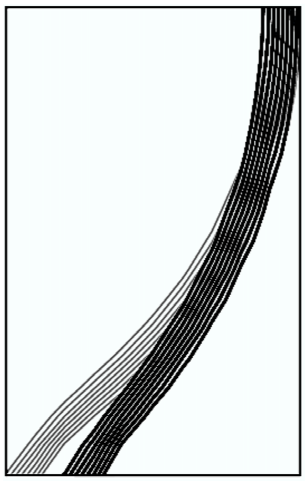

Figure 3.6: An advancing drop: the lines starting nearer to the rotation axis (i.e. on the left) represent the rejected configuration in which the contact zones between liquid and solid plates are artificially pinned.

the lower plate: the contour lines of the 0.5 level curve of ϕ at several time steps of the simulation are plotted, superimposing them. The picture shows clearly the initial variation of the contact angle and the subsequent advancing of the front with a constant contact angle equal to the advancing angle.

3.4.3 Drops on an inclined plane: the 2-D case

A 2-D simulation represents a portion (of unit thickness) of a 3-D geometry invariant in the orthogonal direction. This, admittedly artificial, scenario of a cylindrical drop is already quite rich and interesting. In Figure 3.7 a typical situation is shown: the

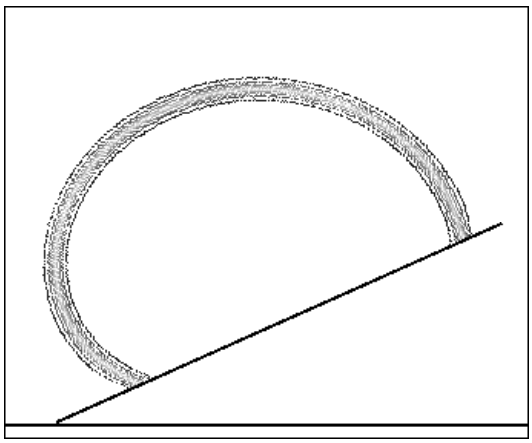

Figure 3.7: A phase field representation of a drop in equilibrium on an inclined plane. Equilibrium is an effect of the hysteresis of the contact angle.

hysteresis of the contact angle allows for the equilibrium of a drop on an inclined plane. In the simulations we change the inclination of the plane and we follow the changes in shape up to the limit configuration in which the drop starts to move and roll down. In Figures 3.8-3.11 the effect of gravity on drops of different volumes is clearly visible. In these graphs only the contour line $\phi = 0.5$ is drawn and the lines coming from different inclinations of the plane are superimposed.

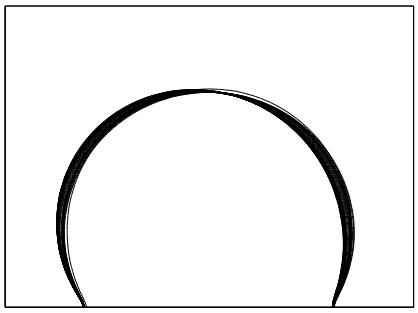

Figure 3.8: For $\bar{d} = 2.2$, the drop is stable up to 90°.

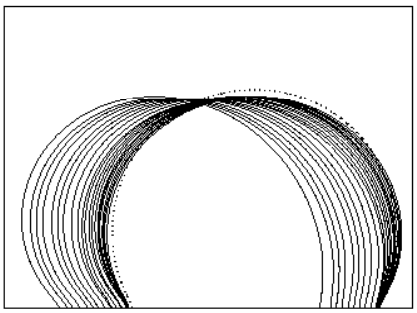

Figure 3.9: For $\bar{d} = 3.6$ the drop is stable up to 60°.

The simulations represent water drops in air ($\sigma_{LV} = 73\,mN/m$ and therefore $\kappa^{-1} = 2.7mm$) on a hydrophobic solid with $\theta^Y = 120°$; the contact angle hysteresis is set to $\pm 15°$.

Like in a laboratory experiment, the initial condition for the simulation is important: the first calculation is the drop of the desired volume in the absence of gravity and with Young angle (dotted line in the pictures). Then gravity and dissipation are added at the same time. As a consequence, the drop stays symmetric but has a contact angle larger than the original one. The bigger the volume, the higher is the gravitational effect and thus the wider the angle. The effect of this is also visible when we incline the plane: if the size of the drop is over the capillary length, the drops change their shape and their wet zone. With this preparation, drops move first the advancing zone: indeed the starting angle is closer to the advancing angle and the drops will reach it sooner.

We increase the inclination of the plane slowly in order to simulate a quasi-static evolution of the type described in Section §2.4. At each step we increase the angle by 3°. In the pictures we superimpose the equilibrium configurations, as long as they exist. This means that after the last frame the drop falls dawn, because gravity overcomes the dissipation and the quasi-static model cannot describe what

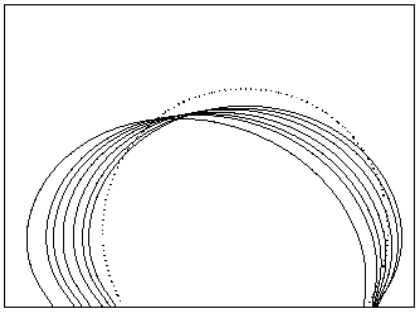

Figure 3.10: For $\bar{d} = 5.8$ the limit of stability is 18°.

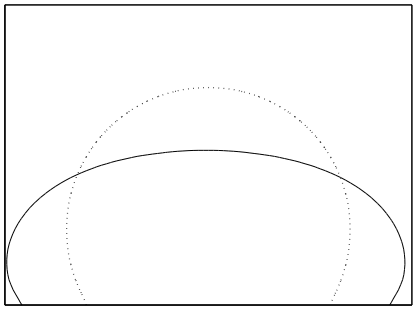

Figure 3.11: For $\bar{d} = 10.9$ the drop falls already at 3°.

is happening next.

In order to compare our results with the results of 3D experiments, we consider an auxiliary parameter. We introduce $\bar{d}$ as the diameter of the sphere whose volume is equal to that of our cylindrical drop. The pictures shows that for values less than the capillary length the gravity effects are not visible. For $\bar{d} \simeq \kappa^{-1}$ something moves, but the detachment is not apparent. Above this critical size the drops are flattened by gravity, they fall earlier, and with a smaller inclination of the plane.

3.4.4 Pillars

Wetting phenomena on a (microscopically) rough surface have been the object of intense recent studies (see [17] and the references therein). Two models are used to interpret the experimental evidence: the Cassie-Baxter and the Wenzel one.

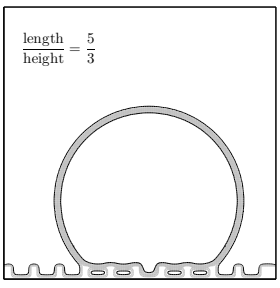

Figure 3.12: In the initial configuration the drop fills the central hole, but it can jump to the next pillars.

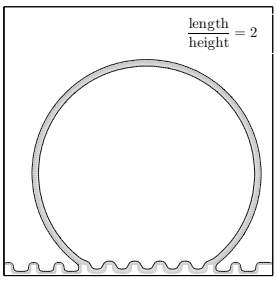

Figure 3.13: By slightly decreasing the height of the pillars the situation changes completely: this drop is in the Wenzel state.

In the first the main assumption is that the liquid phase sees only the top of the asperities of the solid phase, leaving some vapor in the holes under it. The Wenzel model is based on the opposite scenario: the liquid fills all the cavities of the solid. This difference produces different predictions on the advancing and the receding contact angle.

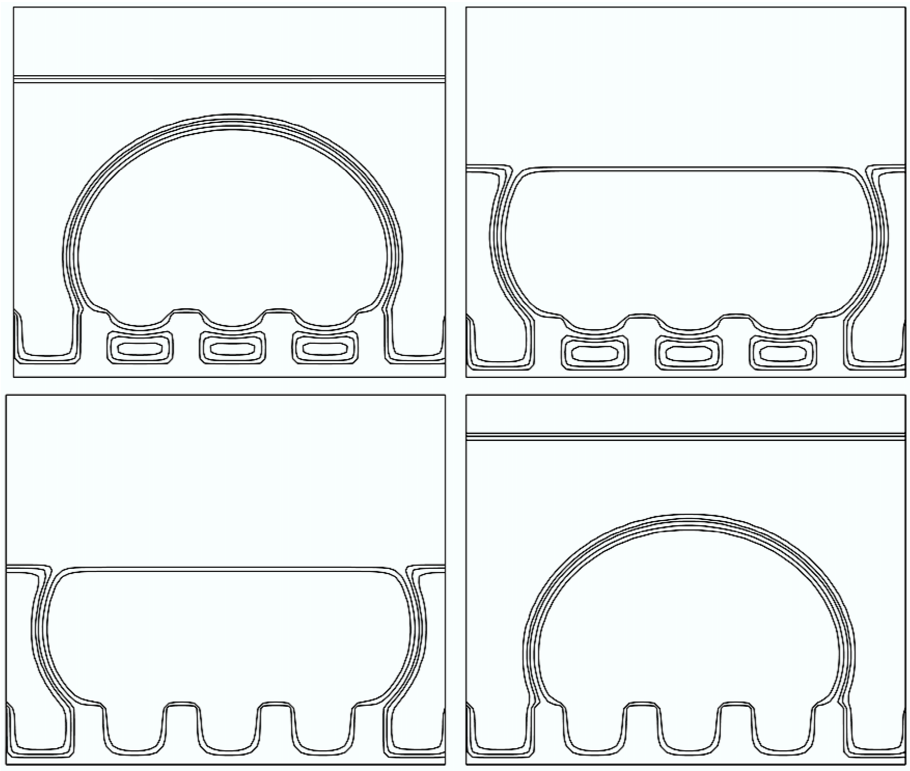

Figure 3.14: Compression induces a meta-stabile Wenzel state on a Cassie-Baxter drop.

The algorithm proposed can capture these behavior. Here we present the results in the 2D case. In Figures 3.12 and 3.13 a drop is placed over a periodic array of pillars. Increasing the drop volume, the liquid can fill the holes or it can jump them. For $\theta^Y = 120°$, theoretical predictions based on homogenization theory [2] say that absolute minimizers will jump if $a/b \leq 2$, where a is the width of the hole and b its height. Our results are very close to that value. The slight disagreement is explained by the fact that an advancing drop with a thick interface "foresees" the contact with the next pillar.

An important remark is the following. This implementation of the method limits us to "small" simulations. This forces us to work with drops of a size comparable to that of the pillars and excludes from our results the analysis of the implications on

the behavior of drops of macroscopic sizes on microscopic pillars, which in typical applications are a few micrometer in size.

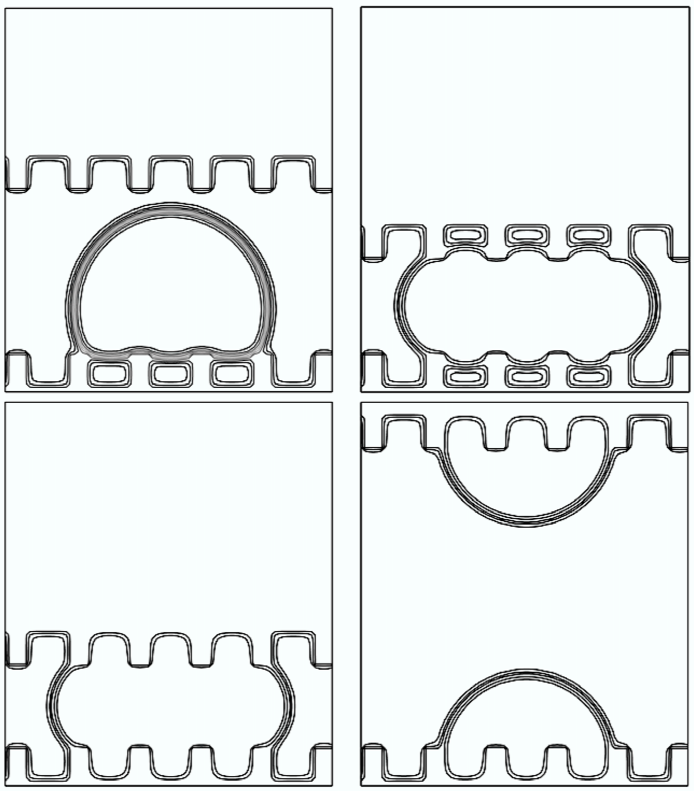

Figure 3.15: Compression between two rows of pillars. Notice the splitting of the drop.

In spite of these limitations, we can still reproduce a very rich range of interesting physical phenomena, related to stability and metastability of capillary drops on rough surfaces. A first interesting situation is the one described by Lafuma and Quéré in [34]: even in a geometry where the solid roughness would produce a Cassie-Baxter energy minimizing state, a Wenzel state can be reached by imposing an external force. Moreover when this force is relaxed this final state is maintained, reflecting its (meta)-stability. For large drops, gravity is a strong enough force to produce this effect, while the technique of the squeezing plates can achieve the same goal for any drop size. The results obtained by this second "technique" are shown in Figures 3.14 and 3.15. In the first group of pictures the upper plate is flat, while in the second group it is rough. Both situations allows for the transition between the two regimes, but the final configuration is different: drops adhere stronger on rough surfaces (if they are in a Wenzel regime [34]) and the strength of this bond

can even allow for a splitting of the drop.

Another interesting experiment is described by Callies and Quéré in [12]. They put a large drop on a rough surface that admits as ground state the Wenzel one. But the small curvature of such a large drop allows to observe a metastable Cassie-Baxter state. They let the drop evaporate and when a critical size is reached, a sudden change in the shape is observed: due to the larger curvature of the smaller drop, the water fills the solid roughness and a large change in the contact angle is produced. In Figure 3.16 and 3.17 a numerical version of a very similar experiment is shown.

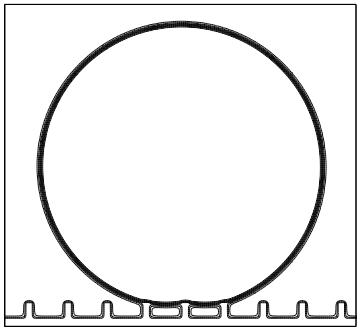

Figure 3.16: With a low curvature we can observe a C-B metastable state.

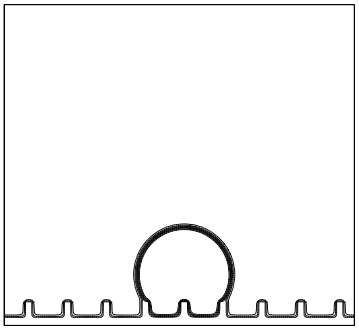

Figure 3.17: Decreasing the volume and so increasing the curvature, the Wenzel state is reached

Chapter 4

WETTING: Multigrid methods and 3D simulations

4.1 Introduction

A 3-D simulation needs a more careful usage of available computing resources: simply adding the third direction, the basic grid passes from 10^4 to 10^6 degrees of freedom. Moreover, as remarked above, an increase in the detail of the description in the neighborhood of the solid surface is desirable for at least a couple of reasons: a better resolution of wet and dry zone; the possibility to draw more realistic asperities (pillars) on it. The first answer to these questions, without changing completely the approach to the problem (for example, passing to finite elements), is an adaptive mesh refinement. The idea is to have a very fine grid only where needed (the solid-liquid and liquid-vapour interfaces) and a hierarchy of levels of increasing grid spacing joining that zone with the coarse underlying grid. Adaptivity, namely, the possibility to create or to destroy computational nodes accordingly with the evolution of the simulation is another important feature.

There is a large literature on adaptive mesh refinement and libraries of software that helps the implementation of the method. However, each specific problem and solution algorithm has its own peculiar features and the general ideas have to be adapted to the specific case. A first example of this is the criterion for selecting the zones that need to be refined: a static refinement is needed to cover the solid surface, while a dynamic refinement will follow Σ_{LV}, driven by the computed value of ϕ. The liquid-vapour interface is characterized by the transition layer between the two values prescribed by the potential W, and therefore we perform the refinement

over the computational nodes where $0.05 \leq \phi \leq 0.95$. The regridding procedure, i.e. the creation of a new hierarchy of levels according to the evolution of the simulation, is computationally demanding and introduces errors in the simulations (it is based on interpolation). We handle this problem by regridding with a decreasing frequency that follows the convergence of the gradient flow (see (3.2)).

In what follows the main elements composing the multigrid environment and the result obtained within it are presented. The construction is based on the work done for the 2D case and the experience gained in that framework. The presentation will focus only on the new tools, namely, the grid hierarchy, the *V cycle* and the *Samrai* code. The precise accordance of the computed with the observed limit angle for a drop on an inclined plane reveals already the capabilities of the proposed strategy, but we expect satisfactory results from the developing studies on possible metastable states of a drop deposited on a textured rough surface.

4.2 Grid hierarchy

Starting on a coarsest grid made of $100 \times 100 \times 100$ nodes (or cells) a hierarchy of refinement levels is built following a few basic rules in order to guarantee easy handling. The main requirements are the following:

- the refinement ratio (the ratio between the grid spacing in two adjacent levels; we set a ratio of 2) must be kept constant passing from one level to the next finer one;
- levels must be correctly nested, namely, level i must share its boundary only with level $i-1$ and $i+1$;
- levels must be composed by regular blocks of refined cells so that their boundary results flat.

Different strategies are admissible, but at the expense of a heavier code and a much more complicated strategy of communication between levels, which is the most delicate issue in a multigrid approach.

Interpolation techniques, preserving the second order accuracy of the finite difference approximation of the Laplacian across a level boundary, are described in [37] and [57]. This is the approach followed in the present work. The Laplacian will be described through the fluxes of the phase function ϕ. In each coordinate direction,

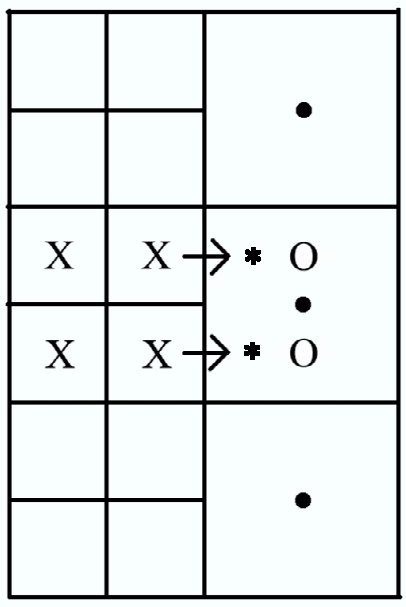

Figure 4.1: A 2D scheme for the interpolation across a coarse-fine boundary. The values corresponding to the positions labeled by O are obtained through quadratic interpolation applied to the values in the black points. These new values together with those in X positions are interpolated to produce the values in *, the ghost cells of this fine level. The arrows represents the top and bottom fluxes.

say x for simplicity, we put:

$$\left(\frac{\partial^2\phi}{\partial x^2}\right)_i = \left(\phi_{i+\frac{1}{2}} - \phi_{i-\frac{1}{2}}\right)/h, \tag{4.1}$$

where h is the grid spacing, and

$$\phi_{i+\frac{1}{2}} = \frac{1}{h}\left(\phi_{i+1} - \phi_i\right) \tag{4.2}$$

$$\phi_{i-\frac{1}{2}} = \frac{1}{h}\left(\phi_i - \phi_{i-1}\right). \tag{4.3}$$

Fluxes across the interfaces between boxes are computed using *ghost cells*. Each box is provided with a layer of fictitious cell that will enter in the six-points stencil of the boundary (real) cells. If the edge between two boxes belonging to the same refinement level is considered, ghost cells are simply copies of the real adjacent cells. Otherwise, two cases are possible: a point on the coarse or on the fine part of the separation plane. Let us consider the first case (see fig. 4.1). The requirement is that fluxes entering and exiting from the fine/coarse interface must balance, therefore we obtain:

$$\left(\frac{\partial^2\phi}{\partial x^2}\right)_i = \left(\phi_{i+\frac{1}{2}} - \phi^*_{i-\frac{1}{2}}\right)/h^c, \tag{4.4}$$

where

$$\phi^*_{i-\frac{1}{2}} = \frac{1}{2}\left(\phi^f_{up} - \phi^f_{down}\right) \tag{4.5}$$

$$\phi^f_{up/down} = \frac{1}{h^f}\left(\phi^{triquad} - \phi^f\right). \tag{4.6}$$

The label *triquad* denotes the fact that the ghost cell of the finer level are computed through a triquadratic (i.e. quadratic in each coordinate direction) interpolation as described in fig. 4.1.

In the second case the ghost cells can be used directly to compute the Laplacian for the finer level, because the triquadratic interpolation guarantees the desired accuracy. Points on the corner of a block need particular attention, but repeating the same procedure, simply shifting the stencil for the interpolation as shown in fig. 4.2, we obtain the right scheme.

A rigorous proof of the achievement of the desired accuracy is very difficult and was not attempted. However the differences between this method and a simple linear interpolation can be seen directly on the simulations: errors would accumulate on the level interfaces and they have no possibility to be recovered (a similar problem occurs at each regrid process, but in few iterations the scheme is able to drop them). A sketch of the proof is revealed by the following argument [37]: our finite difference approximation of the Laplacian implies a division by h^2, and so it would drop the accuracy of a p interpolation to h^{p-2} (for a quadratic interpolation it is known that $p = 3$). But we are doing this process only in a set of codimension one (the interfaces) and we gain one order of accuracy obtaining globally an error of $O(h^{p-1})$. Thus quadratic interpolation should guarantee a second order accuracy of the algorithm.

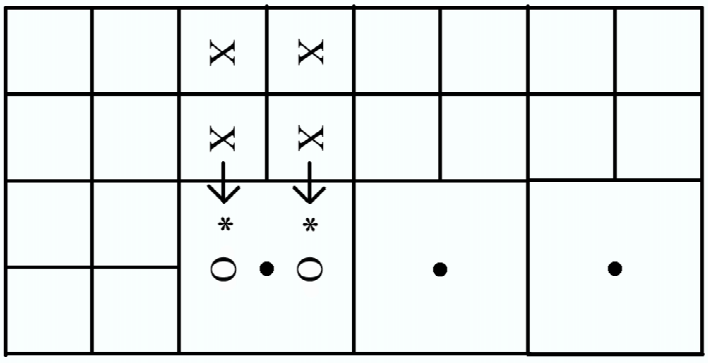

Figure 4.2: The stencil for the first interpolation is shifted in presence of a corner in the coarse-fine boundary.

4.3 V cycle

The core of any multigrid algorithm is the map that governs the progress of the computation, from one level to another one. Many possibilities are described in literature, the most extensively tested one is the so called *V Cycle*. It is an iterative scheme that prescribes at each step to update first the solution on the finest level, then to pass new information down to the coarsest keeping updating ϕ and finally to come back up. Therefore there are two main situations to handle: the passage of the information from a fine to a coarse level and the opposite one, that are the descending and the ascending part of the "V". On each level l, $0 \leq l \leq l_{MAX}$, for each block the procedure can be summarized as follows:

- fill the ghost cells relative to level l and to the boundary with $l+1$ if it exists;
- interpolate on $l-1$ (if it exists) as described above to obtain ghost cells on the fine-coarse interface;
- compute fluxes;
- correct fluxes coming from $l+1$ with the matching condition;
- update the solution on level l (see below);

A peculiarity of the proposed algorithm (3.4) is the splitting procedure adopted to compute the Lagrange multiplier λ. The problem in a multigrid framework is how to handle this extra computational step. Two different solutions to the problem were found: to compute it at each level or to compute it at the end of each V cycle.

In the first case a consistency argument imposes to preserve the volume contained in each level separately. This means that in the third step of the algorithm (3.6) the integral of ϕ and the indicator function should be restricted to the considered level. Indeed, supposing the computational domain as split into only two parts Ω_f and Ω_c it is simple to show the predicted necessary condition for consistency. If ϕ_∞ is a solution, then $-\epsilon\triangle\phi_\infty + \frac{1}{\epsilon}f(\phi_\infty) + \bar{\lambda} = 0$, where f is the derivative of the potential term and $\bar{\lambda}$ is the Laplace pressure. Moreover, performing another iteration of the algorithm on ϕ_∞, the same function should be returned. Putting $\phi^N = \phi_\infty$, the computation on one level, say Ω_c, produces:

$$\phi_c^{N+1} = \begin{cases} \phi^N - \tau\left(-\epsilon\triangle\phi^N + \frac{1}{\epsilon}f(\phi^N)\right) + \tau\lambda_c^N = \phi_\infty - \tau\bar{\lambda} + \tau\lambda_c^N & \text{in } \Omega_c \\ \phi^N = \phi_\infty & \text{in } \Omega_f \end{cases} \tag{4.7}$$

Clearly the requirement is that $\lambda_c^N = \bar{\lambda}$ and the only possibility, if we want to work only inside Ω_c, is to impose:

$$\lambda_c^N = \frac{\int_{\Omega_c}(\phi^N - \phi^{N+\frac{1}{2}})}{|\Omega_c|}. \tag{4.8}$$

Therefore the integral of ϕ on each level remains constant at each iteration, preserving its global value. In this case a high frequency of regridding is needed at the first steps of the gradient flow, in order to divide properly the volume in the different levels. The advantage of keeping the evolution on each level separated from the others is that also τ can assume different values: a faster gradient flow can be imposed to the coarser levels, improving the convergence time.

The contrary happens in the second solution: a single value of λ is computed at each iteration, preserving its physical meaning, at the cost of a τ governed by the finest and slowest levels. However, we can anticipate that this procedure does not need a high rate of regridding and it shows a better stability (a regrid involving many levels is a delicate issue, also for the Samrai code used in this work). The idea is to synchronize the V cycle in such a way that at the end of each loop every level has advanced by the same (fictitious) time $\bar{\tau}$. In a situation with three levels ($0, 1$ and 2), this means to start the V cycle with two iteration on level 2 with a time step $\bar{\tau}/4$, then a step on level 1 with $\bar{\tau}/2$ and one on level 0 with $\bar{\tau}$. The ascending part will be specular to the descending, thus at the end on every level a time $\bar{\tau}$ is "passed". Now a standard splitting step can be performed producing a value of λ common to all levels. Consistency is preserved also within this scheme as a simple calculation similar to the previous one could show.

As already mentioned, the problem is that $\bar{\tau}/4$ in this example should be an appropriate time step for the fine level 2. If condition (3.14) is employed as a formula to predict the value of τ for a given grid spacing h, this scheme will advance on level 0 with a time step that is one half of the optimal one. Numerical evidence shows that this is not a too strong drawback, compared to the error introduced by the regridding procedures needed by the first algorithm. The simulations presented in the following sections are obtained with this second approach.

4.4 Parallel computing platforms

The complex structure of the grid hierarchy, with its ghost and real cell, the interpolations and the indexing of a so large number of degrees of freedom, calls for the

use of an existing ad hoc library. Samrai, a C++ library developed specifically for adaptive mesh refinement was our choice. Moreover, the computational cost (time) of even a single simulation is beyond of the capabilities of a standard computer. Parallelization of the code on Cerbero and Mercurio1 partitions of the high performance computing grid available at Sissa-Democritos was performed, in collaboration with Eng. Carlo De Vittoria.

Samrai is a software library, free for research purposes, developed in the Center for Applied Scientific Computing at Lawrence Livermore National Laboratory [32]. The main help provided by this code is the automatic handling of *patches*: a patch is a block of cells belonging to the same refinement level with rectangular faces. Communication among patches is the basic operation performed by Samrai: ghost cells are filled through data coming from adjacent patches and therefore the computation can ran in a parallel way in different blocks (that will be assigned to different processors). A load balancer is thus necessary and indeed it is provided by the code. The algorithms governing the creation of patches are standard in the literature on adaptive mesh refinement and refer to the original ideas of Berger and Rigotsous [9]. Since they do not interfere with the calculations and since we did not need to modify them, they are not described here in details.

The generation of a new refinement level can be automatic or imposed through the input file governing all the parameters of the simulation. Samrai will nest properly the new level in the existing hierarchy. A routine for regridding is also present, although we found it not very stable. This is another reason to prefer the second scheme for the V cycle. Standard refinement and coarsening operation are integrated in Samrai, while the complex triquadratic interpolation had to be programmed ex novo.

Samrai has been installed on the high performance computing grid available at Sissa-Democritos. A test on the scalability of the code produced the results presented in the table below.

processors	IB	SHMEM	GM
2	10246,50	11367,5	-
4	5531,50	5977,5	-
8	2889	-	2794,5
16	2166.5	-	2064,5
32	1369,5	-	-

These values have to be compared with those relative to one single processor that

is 20023 seconds. The columns refer to the different parallel architectures available: InfiniBand (IB), shared memory (SHMEM) and myrinet (GM). The speedup is almost optimal up to 8 processors, while it decays for larger processors numbers. This is due to the increasing of the communication effort with respect to the computation one. Indeed with two processors the percentage of communication time during the test is of 22.41%, while it becomes $43,17\%$ with 32 processors.

4.5 3D Simulations

The following subsections contain the results obtained with the algorithm just described. The first test regards the hysteresis of the contact angle, that will be responsible for the slip-stick behavior observed in the second one where the solid support of the drop will be inclined. The last simulation concerns the meta-stability states of a drop on a textured solid.

4.5.1 Hysteresis benchmark

The numerical simulation of the hysteresis of the contact angle can be tested against the analytic solution of the corresponding geometric problem, considering also the effects due to the quasi-static evolution we want to investigate. This constitutes a benchmark for the proposed algorithm and guarantees for the accuracy of results obtained in more complicated situations, where an analytic solution is no longer available. A similar test was presented for the 2D case, the results of the 3D one follows the same approach.

In spite of the higher resolution granted by the adaptive mesh refinement technique, the 3D simulations shows similar problems in simulating hysteresis as the 2D ones. It seems impossible to avoid the effects of the diffuse interface model: using two levels of refinement on the solid surface the value of ϵ can be reduced to 0.004. The transition layer consequently reduced its width, but its presence still interferes with the wet-dry division of the solid surface needed by our hysteresis model.

The stabilization trick employed in the 2D simulations is used again to achieve the desired accuracy. Its implementation in this new situation requires only a new strategy for tagging cells in the semi-wet or semi-dry zone: the first step consists in selecting the part of the solid in contact with the liquid; as before the phase value 0.5 is chosen as a discriminant. The boundary of this selection is projected down on the solid surface. A first layer of the semi-wet zone will consist of those cells whose

boundary shares a segment with this projection and lie inside the contact line. A second layer is constructed in the same way forming a annulus of width equal to two cells (this procedure is performed on the refinement level enclosing the transition layer, usually it is the second one). The cells belonging to the semi-dry zone are selected in the same manner but on the exterior of the drop. A detail of the result of this algorithm is presented in fig. 4.3.

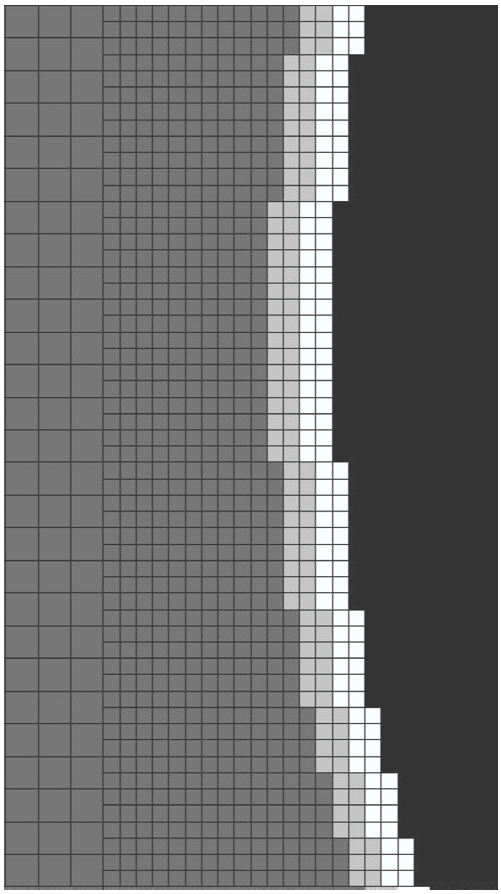

Figure 4.3: A portion of an horizontal slice showing the division of the solid in the wet, semi-wet, semi-dry and dry zone. The boundary of the refined patch is also visible.

Neumann boundary conditions are imposed and the values for the semi-wet and semi-dry zones are exactly the ones described in section §3.4.1. The comparison with the known analytic solution (fig. 4.4, 4.5) reveals the validity of the method that can now be employed to the more interesting situation where gravity come into play.

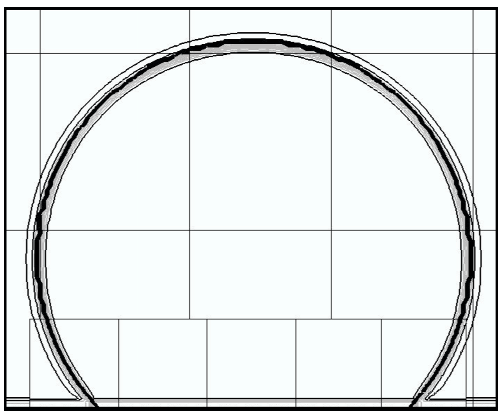

Figure 4.4: A slice of an advancing drop and the division of the computational domain into patches.

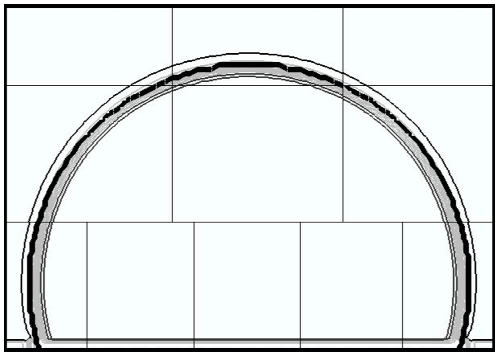

Figure 4.5: A slice of a receding situation. The darker line represents the analytic solution.

4.5.2 Drop on an inclined plane

The situation described in this section is equivalent to of the one discussed in section §3.4.3, but here we consider a 3D drop.

As a comparison we take the experimental data cited in a recent paper [45]. Drops of different size (from $20\mu l$ to $70\mu l$) are deposited on an horizontal plate, which is then inclined. The preparation of the simulation tries to follow what happens in the real experiment: we started from a spherical cap exhibiting the Young contact angle (121°) and then we include the gravity and the dissipation term in the algorithm simultaneously. This decision affects the behavior of the drop during the inclination of the solid support as fig. 4.7 clearly shows: the advancing contact angle is reached with a smaller inclination with respect to the one needed to observe the receding one and therefore the contact line moves mainly in the advancing direction.

In [45] the authors summarize the debate concerning the possible difference between advancing and maximum angle (receding and minimum angle, respectively):

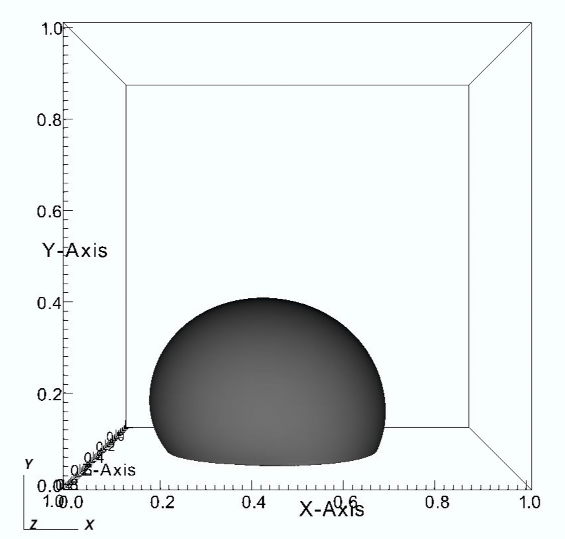

Figure 4.6: A 3D view of the 0.5 contour line of a drop on a inclined plane. In the simulations the plane remains horizontal while the direction of the gravity vector is tilted by the desired angle. Here the inclination is 30°

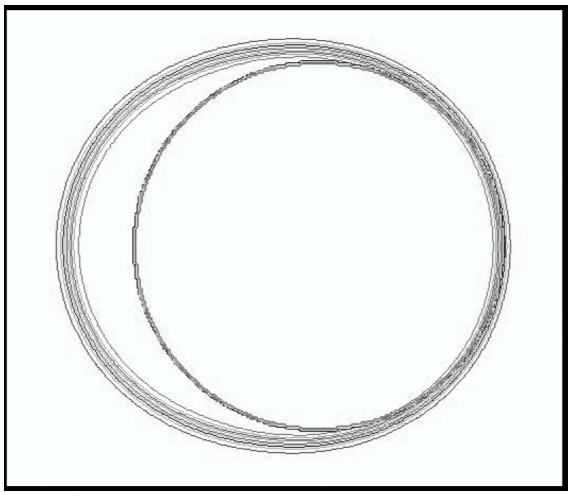

Figure 4.7: The contour lines of a drop on a plane inclined by 30° (an horizontal slice just above the solid). Notice that the right part (the receding one) is almost circular, while the left one (advancing front) is elliptic. The internal circle, included as a reference, is the trace on the plane of the analytic solution corresponding to the same drop in absence of gravity.

the first is the angle predicted by the chemistry of the materials and the fluids involved, the second is the one observed just before the drop slides and it depends also on gravity, dissipation and mechanical equilibrium. The results of our simulation can be employed to investigate deeper the problem, but a method to measure precisely the contact angles in a diffuse interface model is needed first. This could

be a preferred direction for our future work in the field. For the moment we impose through the usual algorithm the values for the advancing (128°) and the receding angle (115°) indicated in the paper and we compute the limit inclination.

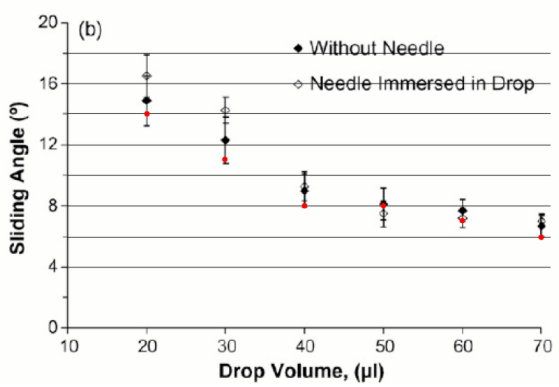

Figure 4.8: Experimental data (black) against computational results (red). We took the background picture from [45].

The values obtained are in good agreement with the experimental ones. In figure 4.8 we superimpose our result over a picture taken from [45]. The red dots correspond to the first angle at which our drop cannot stick on the inclined surface. This means that for lower angles (we tested only integer values) an equilibrium configuration can be reached.

4.5.3 Pillars

The improvement obtained passing from a simple 2D to a 3D simulation is revealed with this example that best exploits the capabilities of the adaptive mesh refinement technique. We want to reproduce the experiment of Callies and Quéré [12]: a drop over a solid surface textured with $12\mu m$ height pillars distributed in such a way that a fakir drop would touch only 1% of their surface. A large drop radius may help the observation of a Cassie-Baxter meta-stable state, but after evaporation of enough liquid the stable Wenzel state is suddenly recovered. Figure 4.9 refers to the first situation, while figures 4.10–4.11 describe the second one. The physical (dimension and spacing) and the chemical (surface tensions) properties of the simulated pillars are exactly the same, but only the large drop exhibits the meta-stable fakir state. Our attempts are now focusing on the reproduction, through a quasi-static evolution, of the whole experiment and on the analysis of any possible dependence of the critical size for the transition with the parameters of the simulation: the surface tensions, the width of the transition layer and the rate at which volume is decreased.

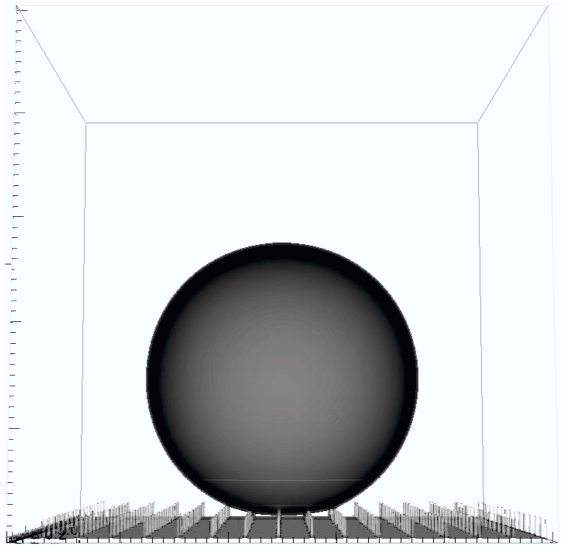

Figure 4.9: A large drop on a meta-stable Cassie-Baxter state. The pillars height is $12\mu m$, their basis is a square of side $2\mu m$. The upper surface represents only 1% of the solid surface.

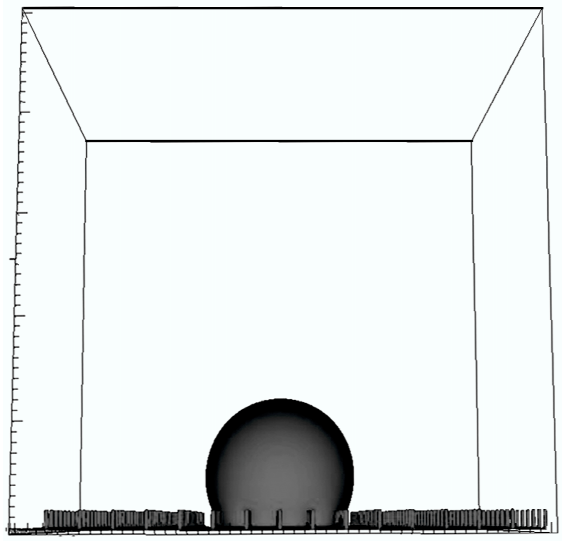

Figure 4.10: A small drop on the same textured surface as fig 4.9 exhibits only the stable Wenzel state.

The size of the computational box showed in the pictures is $0.32mm$ and it would allow us to simulate the final part of Callies and Quéré experiment. Three levels of refinement are necessary to draw the pillars and to simulate the interaction of the solid with the liquid, while we use only one subdivision for the liquid-vapour interface. The total number of patches is 266 for over 40 millions of computational cells. The computation of a single equilibrium state take almost two days of calculation on 64 processors.

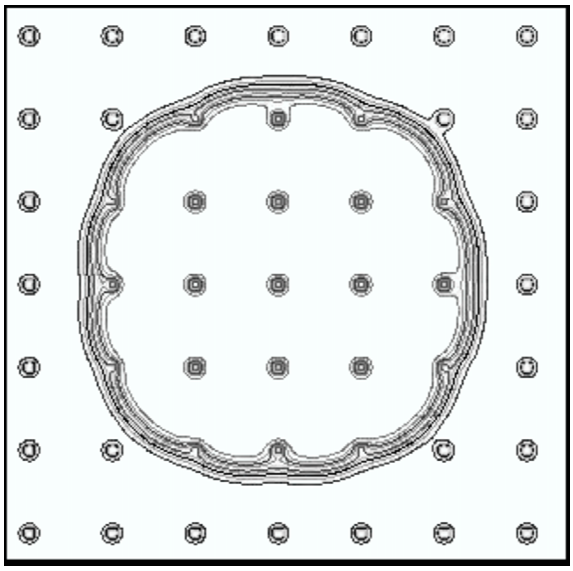

Figure 4.11: An horizontal slice of the little Wenzel drop taken at the level of the pillars basis.

4.6 Perspectives

We want to conclude this exposition with an overview of the framework in which our researches on wetting phenomena are included. The research group lead by prof. DeSimone at Sissa is interested in the possible applications of the rigorous mathematical results developed, especially in the industrial and in the biological field. Two possible applications of the work carried on during my PhD course will be now presented, they refers to these areas.

The code governing the 3D simulation is already fit for simulating a real surface. The dimensions of the pillars of the last example shown recovers exactly those of the support employed by Callies and Quéré. But it is possible to simulate also a non regular pattern, like the one obtained by a scanning of a porous material.

The possible application is the study of a protecting coating for the surface of buildings or of monuments. Exploiting the increasing of hydrophobicity given by the increasing of roughness of the surface and optimizing the effects through appropriate simulations the goal can be achieved.

The geometric model of wetting phenomena involves the curvature of the separation surface between liquid and vapour. More precisely Laplace law prescribes the value of the mean curvature H at each point of this surface with a first order

equation. The models trying to reproduce the shape of a biological bilayer vesicle are very similar, but they ends up with a second order equation. However the expertise gained with the phase field models applied to the wetting problem could be the starting point for the study of such an important problem in biology. We remark that the rigorous proof of the convergence of the diffuse interface model to the sharp one is still missing for this kind of problems.

In the literature there can be found several models for closed vesicles made by two lipid layers. A complete review can be found in [47]. The simplest one is also the most used (although it is valid only in a specific region of the phase space of such a system) and refers to the work of Helfrich [31] who proposed the energy:

$$F_{SC} = \frac{\kappa}{2} \int_{\mathcal{S}} (2H - C_0)^2 \, dA, \tag{4.9}$$

with constrained area and volume of the vesicle. The case in which the parameter C_0 (the so called *spontaneous curvature*) is zero represents the well known Willmore problem, a differential geometry problem still open for high genus surfaces [18]. The shape equation in this case becomes:

$$\triangle H + 2H(H^2 - K) = 0. \tag{4.10}$$

We recall that K is the Gaussian curvature and in the above equation $\triangle$ stands for the Laplace-Beltrami operator.

Numerical studies on phase field models reproducing the equilibrium shape for Helfrich functional exist [19] and use the functional:

$$W(\phi) = \int \frac{k\epsilon}{2} \left| \triangle\phi - \frac{1}{\epsilon^2}(\phi^2 - 1)\phi \right|^2 \, dx. \tag{4.11}$$

A complete $\Gamma-$convergence proof of the asymptotic behavior of this functional is still missing, together with a model for the interaction of the system with a solid surface. Future work on this topic could take advantage from the results described in this thesis.

Bibliography

[1] G. Alberti, G. Bouchitté, P. Seppecher: *Phase transition with Line-Tension Effect*. Arch. Rat. Mech. Anal. 144, 1-46 (1998)

[2] G. Alberti, A. DeSimone: *Wetting of rough surfaces: a homogenization approach*. Proc. R. Soc. A 461, 79-97 (2005)

[3] G. Alberti, A. DeSimone: *in preparation* (2008)

[4] H. Amann , E. Zehnder: *Periodic Solutions of Asymptotically Linear Hamiltonian Systems*, Manus. Math., **32** (1980) 149-189

[5] A. Ambrosetti, V. Coti Zelati: *Periodic solutions of singular Lagrangian systems.* Progress in Nonlinear Differential Equations and their Applications, 10. Birkhäuser Boston, Inc., Boston, MA, 1993. xii+157 pp.

[6] D. Bai and R. Elber: *Calculation of Point-to-Point Short-Time and Rare Trajectories with Boundary Value Formulation*, J. Chem. Theory Comput. 2, 484 (2006).

[7] S. Baldo, G. Bellettini: $\Gamma-$*convergence and Numerical Analysis: an Application to the Minimal Partition Problem*. Ricerche di Matematica 1, 33-64 (1991)

[8] W. Bao, Q. Du: *Computing the ground state solution of Bose-Einstein condensates by a normalized gradient flow* SIAM J. Sci. Comp. 25, 1674 (2004)

[9] M. Berger, I. Rigoutsos: *An Algorithm for Point Clustering and Grid Generation.* IEEE Transactions Systens, Man and Cybernetics, 21 (5), 1278-1286 (1991)

[10] P. G. Bolhuis, C. Dellago, and D. Chandler: *Sampling ensembles of deterministic transition pathways*, Faraday Discussions (110), 421 (1998).

[11] A. Braides: $\Gamma-$*convergence for beginners*. Oxford University Press 2002

[12] M. Callies, D. Quéré: *On water repellency*. Soft Matter 1, 55-61 (2005)

[13] J. B. Campbell: *Finite differences techniques for ring capacitors*. J. Eng. Math., vol 9, No 1, 21-28 (1974)

[14] A. E. Cho, J. D. Doll, D. L. Freeman: *The construction of double-ended classical trajectories*, Chemical Physics Letters 229 (3), 218 (1994).

[15] C. Conley, E. Zehnder: *The Birkhoff-Lewis fixed point theorem and a conjecture of V.I. Arnol'd*, Invent. Math. 73, 33-49, (1983).

[16] R. Czerminski, R. Elber: *Reaction path study of conformational transitions in flexible systems: Applications to peptides*, Journal of Chemical Physics 92 (9), 5580 (1990).

[17] P.-G. De Gennes, F. Brochard-Wyart, D. Quéré: *Capillarity and Wetting Phenomena*. Springer 2004

[18] M. P. Do Carmo: *Differential geometry of curves and surfaces.* Englewood Cliffs, NJ Prentice-Hall (1976).

[19] Q. Du, C. Liu, X. Wang: emphA phase field approach in the numerical study of the elastic bending energy for vesicle membranes. J. Comput. Phys. 198, 450-468 (2004)

[20] G. Dal Maso: *An introduction to* $\Gamma-$*convergence*. Birkhaüser 1993

[21] G. F. Dell'Antonio: *Variational calculus and stability of periodic solutions of a class of Hamiltonian systems.* Special issue dedicated to Elliott H. Lieb. Rev. Math. Phys. 6 (1994), no. 5A, 1187–1232.

[22] J. D. Doll: *Monte Carlo Fourier Path Integral Methods in Chemical Dynamics*, J. Chem. Phys., 82, 80 (1984)

[23] J. D. Doll, R. D. Coalson, D. L. Freeman: *Fourier path-integral Monte Carlo methods: Partial averaging*, Physical Review Letters 55 (1), 1 (1985).

[24] J. P. K. Doye, M. A. Miller, D. J. Wales: *The double-funnel energy landscape of the 38-atom Lennard-Jones cluster*, Journal of Chemical Physics 110 (14), 6896 (1999).

[25] A. DeSimone, N. Grunewald, F. Otto: *A new model for Contact Angle Hysteresis*. Networks and. Heterogeneous Media, vol. 2, pp. 211-225 (2007)

[26] W. N. E, W. Q. Ren, E. Vanden-Eijnden: *String method for the study of rare events*, Physical Review B 66 (5), 052301 (2002).

[27] R. Elber, A. Ghosh, A. Cardenas: *Long Time Dynamics of Complex Systems*, Accounts of Chemical Research 35 (6), 396 (2002).

[28] R. P. Feynman, A. R. Hibbs: *Quantum mechanics and path integrals*, New York McGraw-Hill 1965, xiv+365p.

[29] R. Finn: *Equilibrium Capillary Surfaces*. Springer 1986

[30] R. E.Gillilan, K. R. Wilson: *Shadowing, rare events, and rubber bands. A variational Verlet algorithm for molecular dynamics*, J. Chem. Phys. 97, 1757 (1992)

[31] W. Helfrich: *Elastic properties of lipid bilayers membranes: theory and possible experiments*. Z. Naturforsch. C, 28, 693-703 (1973)

[32] R. D. Hornung, S. R. Kohn: *Managing application complexity in the SAMRAI object-oriented framework*. Concurrency Computat.: Pract. Exper. (2002)

[33] H. Jonsson, G. Mills, K. W. Jacobsen, in *Computer Simulation of Rare Events and Dynamics of Classical and Quantum Condensed-Phase Systems – Classical and Quantum Dynamics in Condensed Phase Simulations*, edited by B. J. Berne, G. Ciccotti, and D. F. Coker (World Scientific, Singapore, 1998), pp. 385.

[34] A. Lafuma, D. Quéré: *Superhydrophobic states*. Nature Materials 2, 457-460 (2003)

[35] L. Lapidus, G. F. Pinder: *Numerical Solution of Partial Differential equations in Science and Engineering*, Wiley (1982)

[36] D. Laugwitz: *Differential and Riemannian Geometry*. Academic Press, New York (1965)

[37] D. F. Martin, K. L. Cartwright: *Solving Poisson's Equation using Adaptive Mesh Refinement*. Technical Report M96/66 Univ. of California, Berkeley Electronic Research Lab (1996)

[38] L. Modica: *Gradient theory of phase transitions with boundary contact energy.* Ann. Inst. H. Poincaré Anal. Non Linéaire 5, 497 (1987)

[39] L. Modica, S. Mortola: *Un esempio di* $\Gamma-$*convergenza.* Boll. Un. Mat. It. B 14 285-299 (1977)

[40] K. Mueller:*Reaction paths on multidimensional energy hypersurfaces.* Angew. Chem., 19, 1-13 (1980).

[41] R. Olender, R. Elber: *Calculation of classical trajectories with a very large time step: Formalism and numerical examples*, Journal of Chemical Physics 105 (20), 9299 (1996).

[42] D. Passerone: *Computing the density of paths in complex systems*, Journal of Chemical Physics 124 (13) (2006).

[43] D. Passerone, M. Ceccarelli, M. Parrinello: *A concerted variational strategy for investigating rare events*, Journal of Chemical Physics 118 (5), 2025 (2003).

[44] N. A. Patankar: *On the modeling of hydrophobic contact angles on rough surfaces.* Langmuir 19, 1249-1253 (2003)

[45] Pierce E., Carmona F. J., Amirfazli A.: *Understanding of sliding and contact angle results in tilted plate experiments.* Colloids and Surfaces A, 323, 73-82 (2008)

[46] Y. Saad: *Iterative methods for sparse linear systems* (2nd edition), SIAM, 2003.

[47] U. Seifert: *Configuration of fluid membranes and vesicles.* Advances in Physics, vol 46, 1, 13-137 (1997)

[48] P. Seppecher: *Moving contact lines in the Cahn-Hilliard theory.* Int. J. Engng. Sci. Vol. 34, No. 9 , pp.977-992 (1996)

[49] J. C. Strikwerda: *Finite Difference Schemes and PDE.* SIAM 2004

[50] L. Tonelli: *Sulle orbite periodiche*, Rend. R. Accad. dei Lincei, XXI-1 (1912) pp. 251-258 and 332-334.

[51] A. Turco: *Tecniche Variazionali e Indagine Numerica per problemi di Dinamica Molecolare*, degree thesis, Univ. Padova (2004)

[52] A. Turco: *Adaptive Mesh Refinement applied to the Phase Field simulation of Wetting Phenomena*. Preprint Sissa 58/2008/M

[53] A. Turco, F. Alouges, A. DeSimone: *Wetting on rough surfaces and contact angle hysteresis: numerical experiments based on a phase field model*. Preprint Sissa 91/2007/M

[54] A. Turco, D. Passerone, F. Cardin: *Tonelli principle: finite reduction and fixed energy molecular dynamics trajectories*. MMS, to appear (2008)

[55] X. Yang, J. J. Feng, C. Liu, J. Shen: *Numerical simulations if jet pinching-off and drop formation using an energetic variational phase-field method*. J. Comput. Phys. 218, 417-428 (2006)

[56] F. G. Wang, D. P. Landau: *Efficient, Multiple-Range Random Walk Algorithm to Calculate the Density of States*, Physical Review Letters 86 (10), 2050 (2001).

[57] S. Wise, J. Kim, J. Lowengrub: *Solving the regularized, strongly asinotropic Cahn-Hilliard equation by ab adaptive nonlinear multigrid method*. J. Comput. Phys. (2007)

[58] L. Zanelli, P. Guiotto, F. Cardin: *Integral Representations of the Schrödinger propagator* Reports on Mathematical Physics, to be printed (2008)